Investigation of the efficacy of the UV/Chlorine process for the removal of trimethoprim Effects of operational parameters and artificial neural networks modelling

Teo, Ying Shen ; Jafari, Iman ; Liang, Fei ; Jung, Youmi ; van der Hoek, Jan Peter; Ong, Say Leong ; Hu, Jiangyong

DOI
10.1016/j.scitotenv.2021.152551

Publication date
2022

Document Version
Final published version

Published in
Science of the Total Environment

Citation (APA)
Teo, Y. S., Jafari, I., Liang, F., Jung, Y., van der Hoek, J. P., Ong, S. L., & Hu, J. (2022). Investigation of the efficacy of the UV/Chlorine process for the removal of trimethoprim: Effects of operational parameters and artificial neural networks modelling. *Science of the Total Environment*, *812*, 1-14. Article 152551. https://doi.org/10.1016/j.scitotenv.2021.152551

Science of the Total Environment 812 (2022) 152551

Contents lists available at ScienceDirect

Science of the Total Environment

journal homepage: www.elsevier.com/locate/scitotenv

Investigation of the efficacy of the UV/Chlorine process for the removal of trimethoprim: Effects of operational parameters and artificial neural networks modelling

Ying Shen Teo [a], Iman Jafari [a], Fei Liang [b], Youmi Jung [a], Jan Peter Van der Hoek [b], Say Leong Ong [a], Jiangyong Hu [a,*]

[a] Department of Civil & Environmental Engineering, National University of Singapore, 1 Engineering Drive 2, Singapore 117576, Singapore
[b] Department of Civil Engineering and Geosciences, Delft University of Technology, Stevinweg 1, 2628 CN Delft, the Netherlands

HIGHLIGHTS

- UV/Cl_2's application at alkaline pH was harnessed via higher wavelengths UV-LEDs.
- At alkaline pH, UV/Cl_2 removed more PPCPs that are amendable to $ClO^{\bullet}$ degradation.
- Trimethoprim removals via chlorine photolysis worked best at UV (275)/Cl_2.
- Congruency was achieved when ANN modelling was applied to predict R_{RCS} and $R_{HO^{\bullet}}$.
- ANN modelling proved that exposure time had the highest relative contribution.

GRAPHICAL ABSTRACT

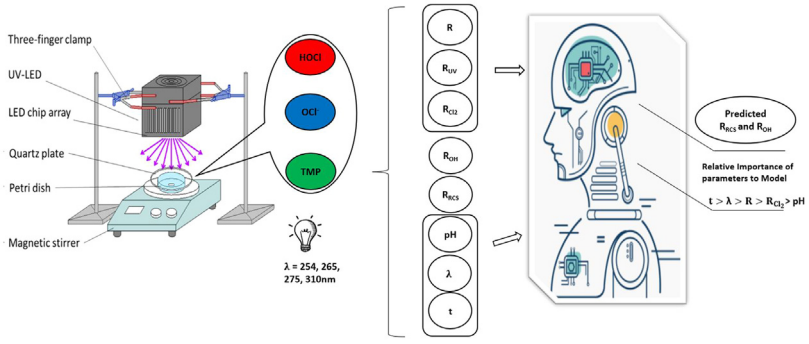

ARTICLE INFO

Article history:
Received 18 October 2021
Received in revised form 13 December 2021
Accepted 15 December 2021
Available online 21 December 2021

Editor: Jay Gan

Keywords:
Ultraviolet light-emitting diodes (UV-LED)
UV/Chlorine
Trimethoprim
Reactive chlorine species (RCS)
Machine learning
Artificial neural network modelling

ABSTRACT

The UV/Cl_2 process (also known as chlorine photolysis, which is the combination of chlorine and simultaneous irradiation of UV light) is conventionally applied at acidic mediums for drinking water treatment and further treatment of wastewater effluents for secondary reuse. This is because the quantum yield of $HO^{\bullet}$ from HOCl ($\phi_{HO^{\bullet},\,254} = 1.4$) is greater than the one from OCl^- ($\phi_{HO^{\bullet},\,254} = 0.278$) by approximately 5 times. Moreover, chlorine photolysis in acidic mediums also tends to have lower radical quenching rates than that of their alkaline counterparts by up to 1000 times. The aim of this research is to investigate the applicability of the UV/Cl_2 process by assessing its efficacy on the removal of trimethoprim (TMP) at not only acidic to neutral conditions (pH 6-7), but also alkaline mediums (pH 8-9). At alkaline pH, free chlorine exists as OCl^- and since OCl^- has a higher molar absorption coefficient as compared to HOCl at higher wavelengths, there would be higher reactive chlorine species (RCS) formation and contribution. TMP removal followed pseudo-first order kinetics and depicted that a maximum fluence based constant ($k_f' = 0.275\ cm^2/mJ$) was obtained using 42.25 μM (3 mg/L) of chlorine at pH 9, with an irradiation of 275 nm. At alkaline conditions, chlorine photolysis performance followed the trend of UV (275)/Cl_2 > UV (265)/Cl_2 > UV (310)/Cl_2 > UV (254)/Cl_2. RCS like $Cl^{\bullet}$, $Cl_2^{-\bullet}$ and $ClO^{\bullet}$ contributed to the degradation of TMP. When the pH was increased from 6 to 8, contribution from hydroxyl radicals ($HO^{\bullet}$) was decreased whilst that of RCS was increased. Application of UV (310)/Cl_2 had the highest $HO^{\bullet}$ generation, contributing to TMP removals up to 13% to 48% as compared to 5% to 27% in UV (254, 265, 275)/Cl_2 systems at pH 6-9. Artificial neural networks modelling was found to be able to verify and predict the contribution of $HO^{\bullet}$ and RCS conventionally calculated via the general kinetic equations in the UV/Cl_2 system at 254, 265, 275 and 310 nm.

* Corresponding author.
E-mail address: ceehujy@nus.edu.sg (J. Hu).

http://dx.doi.org/10.1016/j.scitotenv.2021.152551

1. Introduction

Pharmaceuticals and personal care products (PPCPs) encompass organic compounds such as hormones, drugs, and perfumes. These are classified as environmental contaminants (Daughton and Ternes, 1999; Halling-Sørensen et al., 1998) as they are frequently found in wastewater effluents, seawater, and surface waters around the world (Vieno et al., 2007). Traces of PPCPs are also found in drinking water (Houtman et al., 2014) and this only serves to reinforce the said severity of widespread environmental contamination by such PPCPs. Many PPCPs are unamenable to traditional water and wastewater treatment processes such as sand filtration, coagulation, sedimentation and activated sludge processes (Vieno et al., 2007); rendering them to be still physically present in trace amounts when discharged into aquatic environments (Jelic et al., 2011; Sui et al., 2011; Yang et al., 2011).

An example of such PPCPs is trimethoprim (TMP). TMP has been applied to eradicate infectious bacteria because of its high potency and availability as a cheap antibiotic. TMP is usually prescribed alone or in combination with sulfamethoxazole (SMX) for the treatment of human urinary tract infections (Li et al., 2005). TMP is also applied by veterinarians for prevention and direct treatment of infections of poultry and applied as steroids for growth purposes (de Paula et al., 2008). After administration of TMP, nearly 50% of the applied dose is removed as renal and faecal waste - with approximately 20% remaining unchanged (Kolar et al., 2014). Due to such widespread use and application, TMP has become ubiquitous in wastewaters - because it is stable (Yang et al., 2011) and used in large amounts (Hirsch et al., 1999). Subpar TMP removals of under 50% in conventional activated sludge (CAS) and membrane bioreactors (MBRs) processes has led to TMP's frequent detection in various water environments (Batt et al., 2006; Jewell et al., 2016; Le et al., 2018; Radjenović et al., 2009).

Advanced Oxidation Processes (AOPs) are physicochemical oxidative methods, most based on the production and use of hydroxyl radicals ($HO^{\bullet}$) and have been widely employed to deal with PPCPs like TMP. Amongst AOPs, UV/Cl_2 has been compared and preferentially favoured to UV/H_2O_2 due to its effectiveness to remove PPCPs (Fang et al., 2014). Firstly, traditional drinking water treatment processes would contain residual free chlorine in the waters for disinfection purposes. The combination of chlorine and suitable UV-C light source (Fang et al., 2014; Forsyth et al., 2013) can effectively transform chlorine-based disinfection systems into AOPs. Therefore, a UV/Cl_2 system can be established by utilising existing infrastructure without a need for heavy retrofitting in the plant. Secondly, the free chlorine photolysis produces multifarious reactive oxidants - some of which include $HO^{\bullet}$, $Cl^{\bullet}$and O_3 (Buxton and Subhani, 1972; Kläning et al., 1984; Vogt and Schindler, 1992). PPCPs can be removed via multiple oxidative pathways as a result - via direct UV photolysis; direct reaction with HOCl/OCl^- or reaction with oxidative species formed by chlorine photolysis (Ben et al., 2016; Chan et al., 2012; Fang et al., 2014; Forsyth et al., 2013; Jin et al., 2011; Nowell and Hoigné, 1992; Sichel et al., 2011; Wang et al., 2012; Watts and Linden, 2007). Lastly, UV/Cl_2 is more efficient than UV/H_2O_2 in several aspects. Looking purely by merit of quantum yield of $HO^{\bullet}$ ($\phi_{HO^{\bullet}}$) at wavelength of 254 nm, $\phi_{HO^{\bullet},\ HOCl}$ is 1.4 (Table S1, Eq. (R1)) and is greater than $\phi_{HO^{\bullet},\ H_2O_2}$of 1.16 (Goldstein et al., 2007). The scavenging rate of $HO^{\bullet}$ by HOCl (Eq. (1)) is approximately 320 times lower than that by H_2O_2 (Eq. (2)) (Rosenfeldt et al., 2013; Watts and Linden, 2007). Moreover, Feng et al. (2007) posits that the molar absorption coefficient (ε) of free chlorine $\varepsilon_{UV/HOCl,\ 254}$ is approximately 60 $M^{-1}cm^{-1}$ (Fig. S3) at $\lambda = 254$ nm whilst $\varepsilon_{UV/H_2O_2,\ 254}$ is 19.6 $M^{-1}cm^{-1}$ (Barakat et al., 2005). The lower ε of H_2O_2 indicates that it is less efficient at producing $HO^{\bullet}$ after photolysis as compared to HOCl/OCl^-, which results in excessive H_2O_2 dosing (Barakat et al., 2005).

$$HO^{\bullet} + HOCl \xrightarrow{k_{HOCl}} ClO^{\bullet} + H_2O, k_{HOCl} = 8.46 \times 10^4\ M^{-1}S^{-1} \quad (1)$$

$$HO^{\bullet} + H_2O_2 \xrightarrow{k_{H_2O_2}} HO_2\bullet + H_2O, k_{H_2O_2} = 2.7 \times 10^7\ M^{-1}S^{-1} \quad (2)$$

Acidic chlorine photolysis has always superseded its alkaline counterparts. However, more investigations have to be done to improve the applicability of UV/Cl_2 in the alkaline mediums as well. From Table S1, the quantum yield of $HO^{\bullet}$ from HOCl ($\phi_{HO^{\bullet},\ 254} = 1.4$) is greater than the one from OCl^- ($\phi_{HO^{\bullet},\ 254} = 0.278$) by approximately 5 times. (Table S1, Eqs. (R1) & (R2)). Employment of chlorine photolysis in acidic mediums also tend to have lower $HO^{\bullet}$ quenching rates by up to 1000 times. (Table S1, Eqs. (R10) & (R11)) (Fang et al., 2014; Qin et al., 2014). UV/Cl_2 systems employed in alkaline mediums (pH > 7.5) should be irradiated at higher wavelengths to attain the higher rate of photolysis. In alkaline mediums, the dominant chlorine species is OCl^- and it has a molar absorption coefficient (ε_{OCl^-}) higher than ε_{HOCl} in the wavelengths spectra of 255 to 400 nm and peaks at 365 $M^{-1}cm^{-1}$ at 292 nm (Fig. S3) (Feng et al., 2007; Wang et al., 2012). Therefore, at higher irradiation wavelengths, the photolysis of HOCl becomes less pivotal to the efficiency of chlorine photolysis as it absorbs minimal light due to low ε. In the present market, UV-C wavelengths ranging from 255 − 285 nm are now commonly available in the form of light emitting diodes (LEDs) (Chen et al., 2017; Muramoto et al., 2014). The ability of UV-LEDs to emit light at a designated and specific wavelength can enable us to match the emission spectra of free chlorine with the highest molar absorption coefficient - thus making UV/Cl_2 systems more energetically efficient and effective across wider treatment conditions by permuting the wavelengths via the use of UV-LEDs. Moreover, there are multifaceted benefits to the employment of LEDs to water treatment - not only are LEDs sturdier than traditional mercury lamps (Vilhunen and Sillanpää, 2010), they do not contain mercury and hence do not require proper disposal protocols (Chevremont et al., 2013a, 2013b; Close et al., 2006). Therefore, water treatment system designs need not be complex as barriers against mercury leakage are no longer needed, enabling the usage of LEDs in water treatment to gain traction.

In recent years, machine learning methods like Artificial Neural Networks (ANN) have been welcomed in water treatment as a successful and powerful tool to generate predictive models. For instance, Kulkarni and Chellam used ANN to model DBP formation using simulated distribution system data (Kulkarni and Chellam, 2010). McArthur and Andrews applied an ANN data driven modelling approach to predict coagulant dosage in a water treatment plant with high accuracy (McArthur and Andrews, 2015). Giwa, et al. and Karadurmuş, et al. both applied ANN modelling to simulate removal of certain contaminants in electrically enhanced membrane bioreactors (Giwa et al., 2016) and drinking waters (Karadurmuş et al., 2019), respectively. ANN is a mathematical model which its structure, like the human nervous system, consists of several layers and each layer itself consists of several neurons so that each neuron is associated to the neurons in the previous layer through a weighted connection (Fig. 1) (Carvajal et al., 2017). Based on mathematical relationships and algorithms, the network analyses the input data in neuron and then transmits them to the neurons in the next layers and finally computes the desired results. The structure of a simple neuron consisting of three layers called input layer, hidden layer and output layer is shown in Fig. 2. Finding a logical relationship between different parameters without having a predetermined equation is not only time consuming, but also near impossible to acquire should there be non-linear relationships existing between parameters. In this regard, machine learning methods have been effective in many cases - due to their independency of defining the complicated behaviour of substantial process. In this study, ANN was used to determine the importance and relationship amongst UV/Cl_2 process parameters and quantify the TMP removal contributed by reactive chlorine species (RCS) and hydroxyl radicals ($HO^{\bullet}$) in the system. Since the determination of RCS contributions in TMP degradation by UV/Cl_2 systems is assumed to be the subtraction of removal efficiencies by chlorine and $HO^{\bullet}$ from the total removal efficiency of TMP, this may result in underestimation of RCS contribution (Eq. (S12)). There is no contribution by direct photolysis (Eq. (S3)) in TMP degradation by UV/Cl_2 systems. Thus, ANN was applied to not only predict the TMP removal contributed by RCS, but also ascertain if

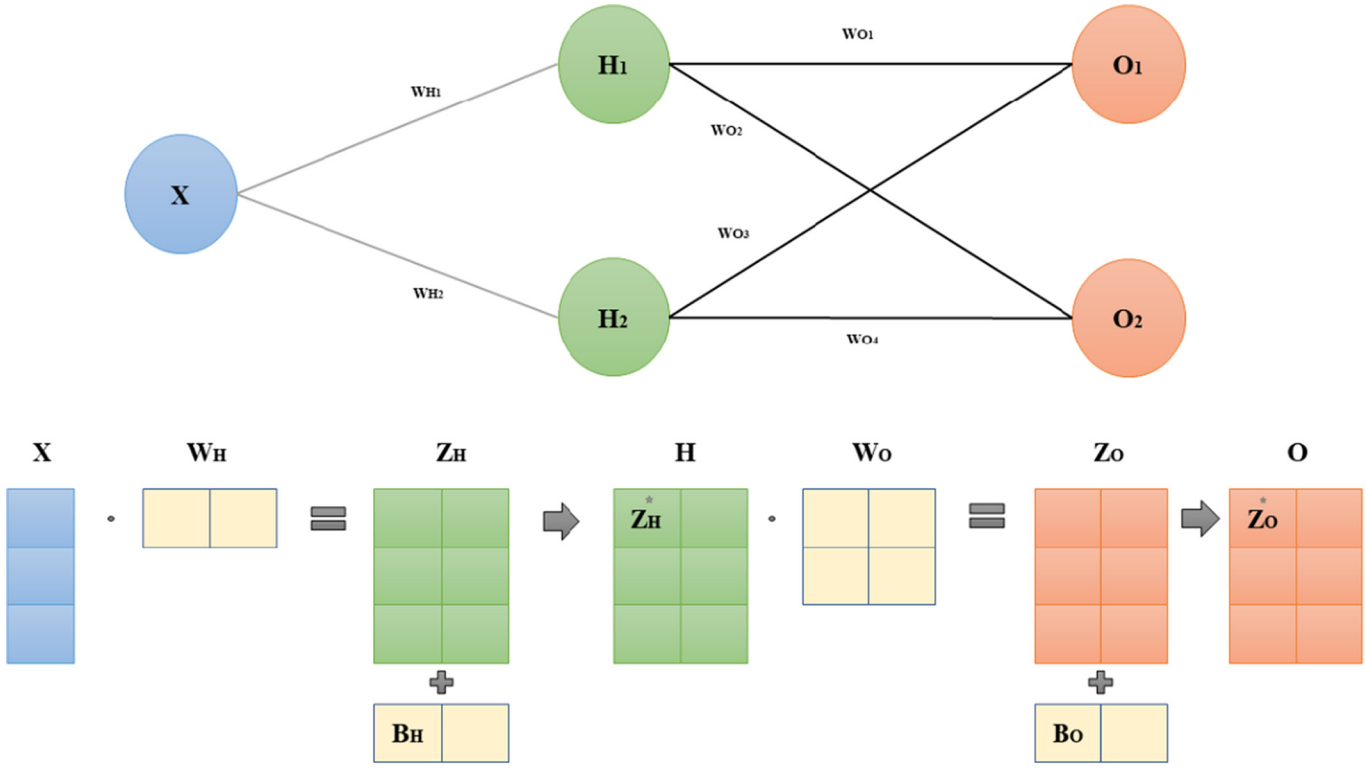

Fig. 1. Weighted connections in ANN.

there is any congruency between the values experimentally determined using Eqs. (S2)–(S12) to that of the values predicted by ANN. Furthermore, as the estimation of TMP removal contributed by $HO^{\bullet}$ is a tedious experimental process, there will be tangible benefits in applying ANN to predict the contribution of $HO^{\bullet}$ in the UV/Cl_2 systems.

Four different UV wavelengths (i.e., 254, 265, 275 and 310 nm) were applied in a UV/Cl_2 AOP system in this study to investigate the kinetics of TMP degradation. The investigation of UV/ Cl_2 AOP with TMP must not be confused with the UV/Chloramine process (see Text S1). The radicals contributing in TMP degradation were also differentiated. Lastly, an ANN

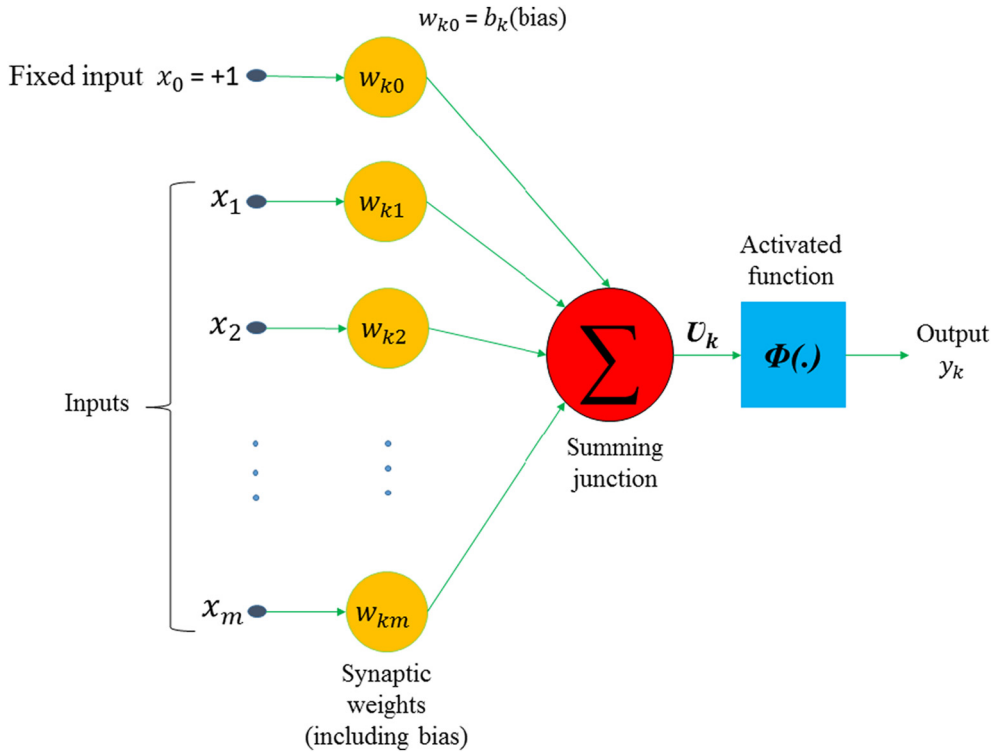

Fig. 2. Structure of a simple artificial neuron.

model was applied to predict and verify the contribution of both HO• and RCS in the UV/Cl_2 system.

2. Materials and methods

2.1. Reagents

All solutions were prepared with reagent-grade chemicals and ultrapure water (18.2M Ω-cm) was obtained from a Milli-Q water purification system (Thermo Scientific, SG). TMP (≥98%), sodium hypochlorite solution (NaOCl, available chlorine 10-15%), sodium thiosulfate ($Na_2S_2O_3$), methanol and formic acid (LCMS grade) were purchased from Sigma-Aldrich (US). Hydrogen peroxide (H_2O_2, 30%) was purchased from Merck (Germany). To calculate the fluence rates of the UV-LED systems via the ferrioxalate actinometry procedure, Titanium (IV) oxysulfate - sulfuric acid (27-31%) solution, ferric sulfate hydrate ($Fe_2(SO_4)_3$, 97%), potassium oxalate monohydrate ($K_2C_2O_4{\cdot}H_2O$, 99%), sodium acetate ($CH_3COONa{\cdot}3H_2O$, 99%), 1, 10-Phenanthroline (99%), hydroxylamine hydrochloride ($NH_2OH{\cdot}HCl$, 99%) and sulfuric acid (H_2SO_4, 95%-98%) were purchased from Sigma-Aldrich (US).

2.2. Experimental procedures

Before conducting any experiments, LP-UV lamps (not including UV-LEDs) were warmed up for approximately 15-20 minutes. Photochemical experiments were all conducted using 25 mL petri dishes, coupled with a magnetic stirrer to provide rapid mixing at the bottom. A quartz plate was used to cover the top of the dish to prevent evaporation during irradiation. Both the 254 nm LP-UV (10 W, Calgon Carbon Corporation, US) and UV-LED 265/275/310 (Taoyuan Electron, Hongkong) systems were placed in the centreline of the petri dish and directly above to irradiate the testing solution as described in Fig. S1. The experiments were conducted at approximately 25° C. The corresponding average UV fluence rate was estimated to be 0.247 mW/cm^2 for the 254 nm LP-UV system - determined via the H_2O_2 actinometry method. As for the UV-LED 265/275/310 systems, the average UV fluence rate were estimated to be 0.177, 0.256 and 0.177 mW/cm^2 (Table S3) via the potassium ferrioxalate actinometry method, respectively (Bolton et al., 2011). The time-based rate constants (k') were used when compiling data solely from UV254 experiments, and fluence based rate constants (k_f') were used when comparing data across all four UV devices (254 nm LP-UV and UV-LED 265/275/310 systems) because they have different UV fluence rates. Therefore, the only basis of comparison will be via the total fluence across the experimental timeframe. The path length used for the experiments was 10.2 cm. All kinetics experiments were consisted of a 20 mL testing solution containing 0.6889 μM (0.2 mg/L) of TMP and 2 mM of PO_4^{3-} buffer (pH 6, 7, 8) and 2mM of glycine-NaOH (0.2M of glycine and NaOH) buffer for pH 9. Experiments were initiated by spiking NaOCl stock solution to give an initial free chlorine concentration of 42.25 − 84.51 μM (3-6 mg/L), which were then exposed to UV irradiation from LP-UV and UV-LED systems. Samples (0.5 mL) were collected at pre-determined experimental intervals and were quenched with $Na_2S_2O_3$ at a molar ratio of $Na_2S_2O_3$ to chlorine of 4:1. Control tests of TMP degradation by direct UV photolysis and dark chlorination were conducted in the absence of chlorine and UV light, respectively. All experiments were conducted at least in triplicate, and samples collected were stored in the dark before LC-MS/MS analysis. Experimentations were also conducted to identify the effect of chlorine dosage and to differentiate the radicals responsible for TMP degradation in both the UV/Cl_2 and UV-LED/Cl_2 systems. For the former, free chlorine concentrations employed were 4.225, 14.08, 42.25 − 84.51 μM (0.3, 1, 3-6 mg/L) and for the latter, nitrobenzene (NB) was used as a radical probe to quantify the roles of reactive species at a concentration of 0.8122 μM (0.1 mg/L) with all other parameters unchanged. To minimise inhibition of the radicals generated in the UV/Cl_2 system due to carbonation in the testing solution at higher pHs (at pH 8.5, all of carbon dioxide dissolved in water is ionised as bicarbonate or carbonate ions), the solution was aerated with oxygen to remove carbon dioxide before starting the chlorine photolysis irrespective of the experimental pH (pH 6, 7, 8, 9). Fresh batches of deionised water were also used immediately for every experiment and the quartz plate

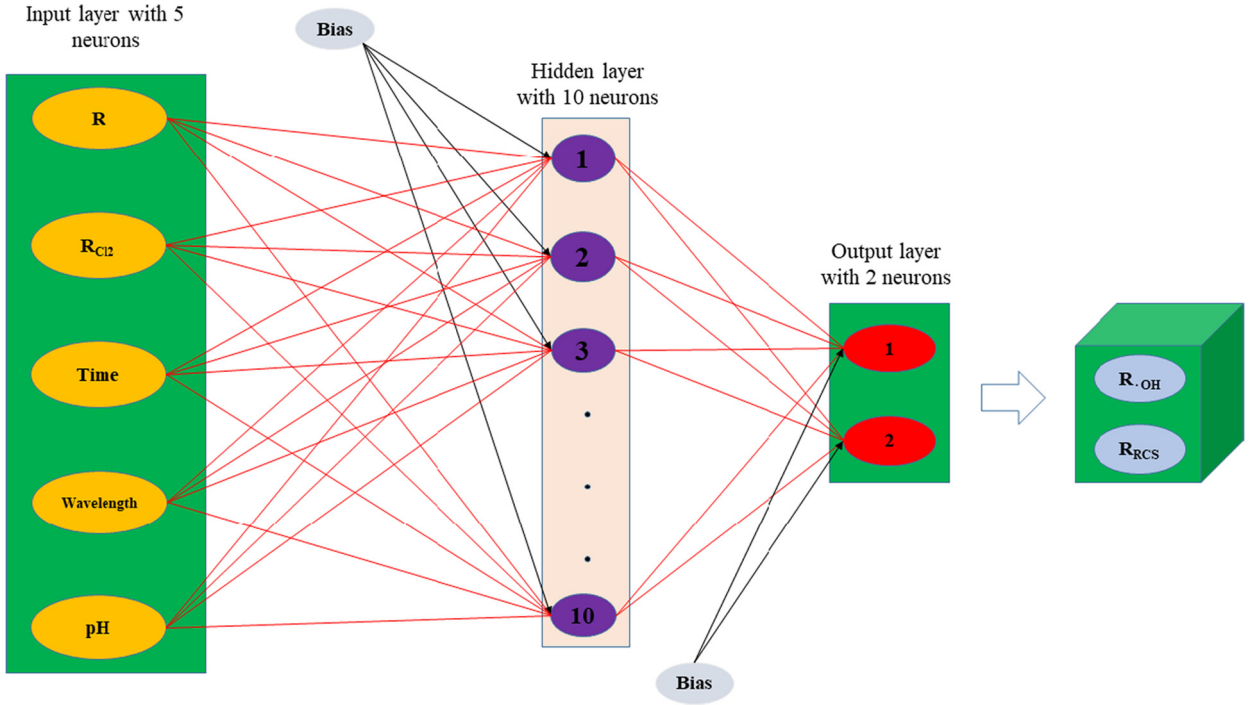

Fig. 3. The optimum structure of a three-layer neural network with 10 neurons in hidden layer and 2 neurons in output layer.

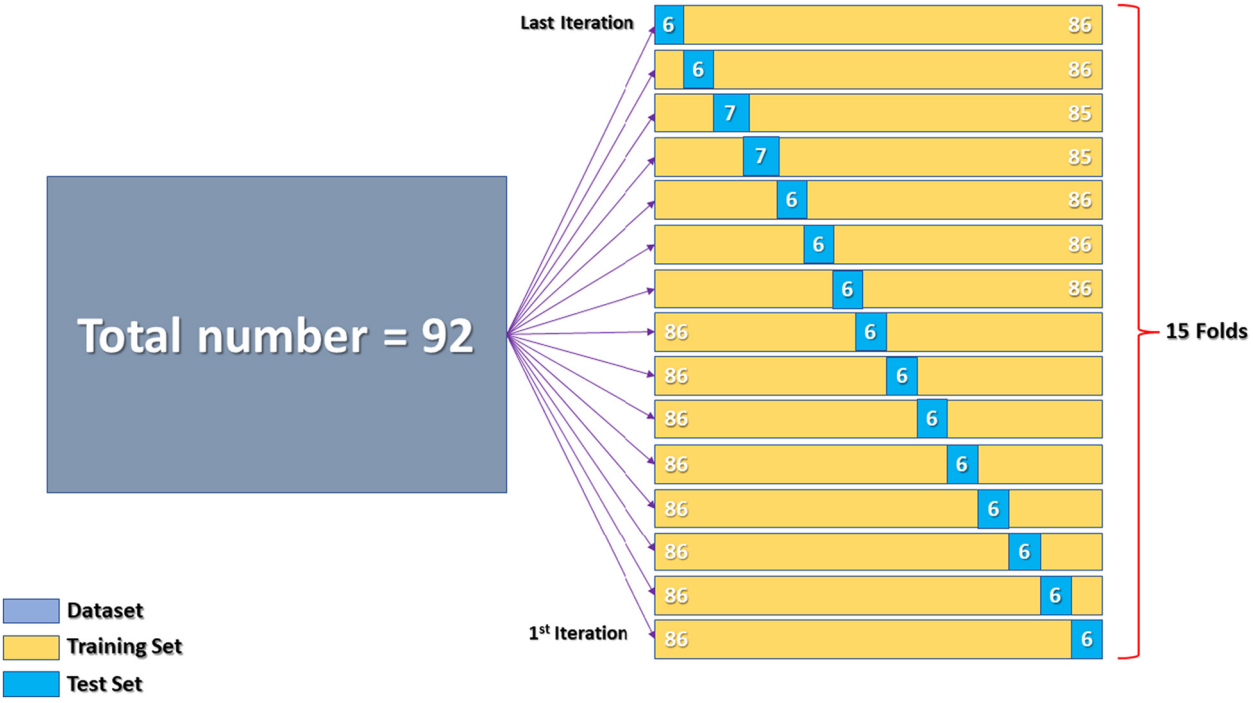

Fig. 4. Description on 15-Fold cross validation step on ANN model generation.

will minimise transfer of carbon dioxide in the atmosphere into the testing solution.

2.3. Analytical methods

The concentration of free chlorine in NaOCl stock solution was periodically standardized by DPD colorimetry (APHA et al., 1999). The solution pH was measured with a pH meter (Schott, SG). The concentration of TMP was determined by a liquid chromatography-double mass spectrometry (LC-MS/MS) system (8030, Shimadzu, Japan) equipped with a Shimpack FC-ODS column (150 × 2 mm, particle size 3 μm) at 40 °C. The mobile phase for the measurement consisted of 0.1% formic acid (A) and methanol (B), at a flow rate of 0.3 mL/min. The retention time for TMP was 4.53 min and the sample injection volume was 10 μL. The gradient program of LC-MS/MS was as follows (A/B, v/v %): 90/10 (0–1 min), decreasing linearly to 10/90 (1–4 min) and 10/90 (4–8 min), increasing linearly to 90/10 (8-8.1 min) and 90/10 (8.1–10 min). During 1-4 min and 8-8.1 min, the value changed linearly with time. The LC was coupled to the MS using electrospray ionization (ESI) in positive mode. Multiple reaction monitoring (MRM) was applied to quantify the protonated product ($[M+H]^+$) with Q1 mass of 291.20 and Q3 mass of 230.10.

2.4. Artificial neural networks modelling

ANN uses previous observations of an element to predict the future values which are not currently existing by assigning a weight coefficient to each neuron to construct the neurons in the next layer. Assuming we have n inputs x_1, x_2,…, x_n, each of the neurons in the next layer (hidden layer) is obtained by assigning a specific weighted coefficient (w_{ij}) to each input data in such a way that the weighted summation of all inputs determines a neuron (y_j) in the next layer (hidden layer) based on Eq. (3).

$$y_j = \sum_{i=1}^{n} x_i w_{ij} \tag{3}$$

After the neurons are constructed in hidden layer, the signals (zj) from hidden layer to output layer are generated using activation function f (t) in which zj = f(yj). Then, similarly, by assigning a specific weighted coefficient to each signal and finding their weighted summation, the output (k) of the neural network is determined based on Eq. (4). The most common types of activation functions are shown in Table S4.

$$k = \sum_{j=1}^{n} z_j w_j \tag{4}$$

To achieve a desirable neural network model, it is necessary to perform steps including data refinement, network architecture, network training and validation (Lange, 1999). In this study, MATLAB R2020a was used to run a three-layer feedforward neural network including one input layer, one hidden layer and one output layer (Fig. 3) with Bayesian Regularization backpropagation training algorithm. For training the model, a dataset with 92 records of R, R_{Cl_2}, t, λ, and pH were used in input layer to predict $R_{HO^\cdot}$ and R_{RCS} in output layer. As the number of data is limited in this study to generate a predictive ANN model, a cross validation method was used as a practical and reliable method to evaluate the predictability of the model

Table 1
Training, validation and test samples and range of unnormalized overall removal efficiency of TMP and unnormalized removal efficiencies of TMP by chlorine, $HO^\cdot$ and RCS in UV/Cl_2 system at λ = 254, 265, 275 and 310 nm at pH 6-9.

Wavelength (λ)	pH	Exposure Time (s)	Number of Data	Overall Rate (R)	R_{Cl2}	$R_{\cdot OH}$	R_{RCS}
254	6-9	60-360	20	0.3406-0.6862	0.0145-0.0585	0.0344-0.1856	0.2289-0.5428
265	6-9	30-180	24	0.2139-0.6879	0.0061-0.0694	0.0115-0.1617	0.1379-0.6304
275	6-9	30-180	24	0.4133-0.6889	0.0043-0.0335	0.0130-0.1399	0.2952-0.6136
310	6-9	30-180	24	0.0577-0.6759	0.0079-0.1141	0.023-0.3333	0.0057-0.3628

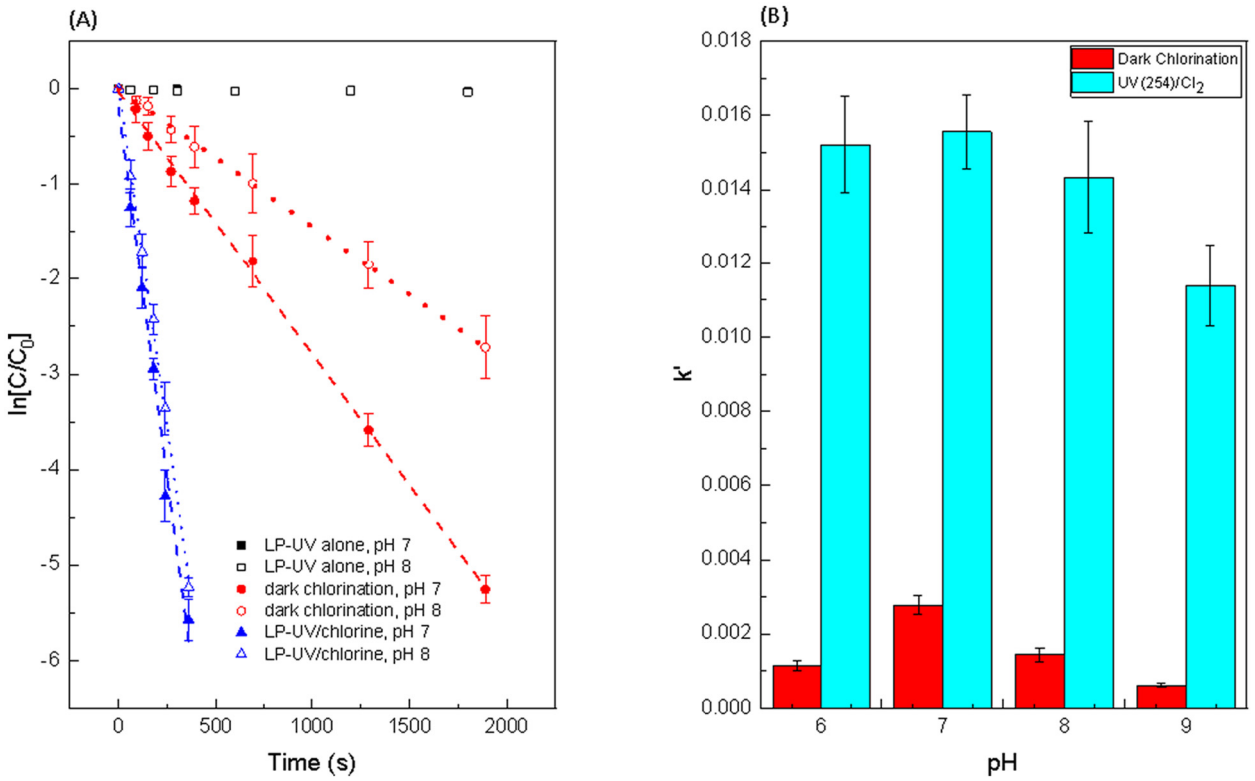

Fig. 5. (A): Comparison of TMP degradation by UV254 irradiation, dark chlorination and UV(254)/Cl_2 process. Conditions: UV intensity: 0.2467 mW/cm^2, $[TMP]_0$ = 0.6889 μM (0.2 mg/L), $[Cl_2]_0$ = 42.25 μM (3 mg/L); (B): Comparison of rate constants of dark chlorination and UV(254)/Cl_2 process. Conditions: UV intensity: 0.2467 mW/cm^2, $[TMP]_0$ = 0.6889 μM (0.2 mg/L), $[Cl_2]_0$ = 42.25 μM (3 mg/L).

on the whole dataset especially when the number of data is limited to predict generalization error without missing any records on the model creation. Hence, a K-Fold cross validation method with 15 number of folds was caried out accordingly on the whole dataset as described in Fig. 4. One separated ANN model was then generated on each fold and the average performance of all 15 generated models was used to report as to better illustrate the generalization error of the final model. In addition, out of these 15 generated ANN models, the best model in terms of the performance on predicting the test set was selected to report its prediction results in this study. The description of the dataset in terms of the number and the numerical range of the experimental parameters that have been used in generating the ANN models are shown in Table 1. Normalizing data before applying them to the network was carried out to make the training faster and to increase the model accuracy. The 'mapminmax' process function (Eq. (5)) was used for both input and output layers so that they fall in the range [-1,1]. Sigmoid transfer function was then used in hidden layer to translate the input signals to output signals (Table S4).

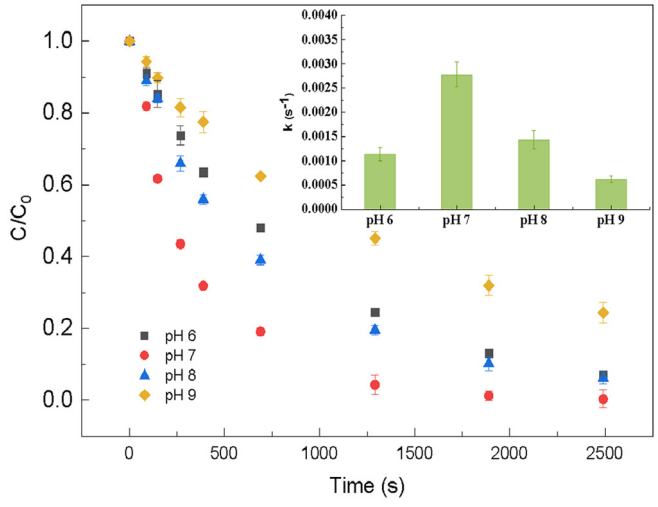

Fig. 6. Effect of dark chlorination on TMP degradation at pH 6-9. Conditions: $[TMP]_0$ = 0.6889 μM (0.2 mg/L), $[Cl_2]_0$ = 42.25 μM (3 mg/L). The inset shows the pseudo first-order rate constants of TMP reacting with free chlorine at pH 6-9.

$$X_{norm} = A_{min} + \frac{X - X_{min}}{X_{max} - X_{min}}(A_{max} - A_{min}) \quad (5)$$

where X_{norm} is the normalised value, X_{min} and X_{max} are the extreme values of the input variables, and A_{min} and A_{max} are the minimum and maximum of normalization scale, respectively.

After normalizing the data in the desired scale using 'mapminmax', the output data were converted to their original range. As the training algorithm in ANN normalizes the input and output data automatically in the system, to avoid re-normalisation of the removal efficiencies in Eq. (S4), Eq. (S3) was used instead:

$$\int_0^t -d[TMP] = R = [TMP]_o - [TMP]_t = \int_0^t k_{Cl_2}[Cl_2][TMP]\,dt + \int_0^t k_{HO^\cdot}[HO^\cdot][TMP]dt + \int_0^t k'_{RCS}[TMP]dt \quad (S3)$$

Eq. (S3) and the corresponding terms will be further defined throughout the paper as:

$$R = R_{Cl_2} + R_{HO^\cdot} + R_{RCS} \quad (6)$$

where R, R_{Cl_2}, $R_{HO^\cdot}$, R_{RCS} are the unnormalised overall removal efficiency of

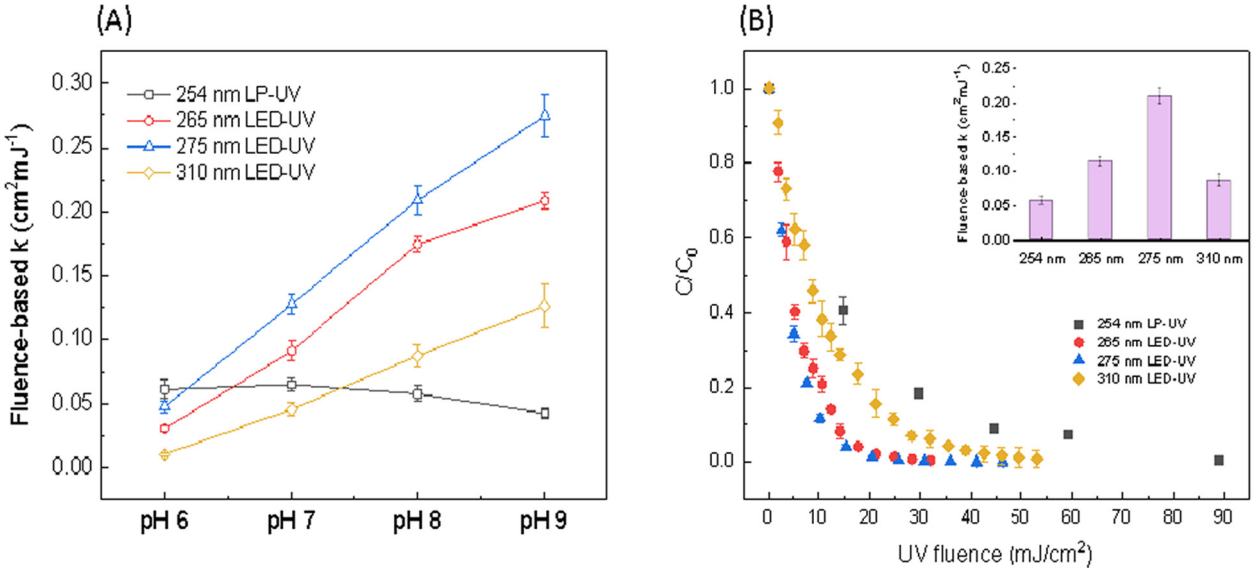

Fig. 7. (A): k_f' of TMP degradation by UV/Cl_2 process at various pHs and wavelengths. Condition: $[TMP]_0$ = 0.6889 μM (0.2 mg/L), $[Cl_2]_0$ = 42.25 μM (3 mg/L); (B): Comparison of TMP degradation by UV/Cl_2 process at λ of 254, 265, 275 and 310. Condition: $[TMP]_0$ = 0.6889 μM (0.2 mg/L), $[Cl_2]_0$ = 42.25μM (3 mg/L), pH 8.

TMP at time t, unnormalised removal efficiency of TMP by chlorine, HO˙ radicals and reactive chlorine species, respectively.

After generating the ANN model, the correlation coefficient (R value) was then assigned to describe the relationship between the experimentally obtained and predicted R_{RCS} values. R value represents how well the two variables are correlated and accordingly, the performance of the model can be evaluated based on this statistical criterion. In addition to correlation coefficient (R value), Mean Squared Error (MSE) was also used in this study to measure the performance of the network according to Eq. (7).

$$MSE = \frac{1}{K}\Sigma_{i=1}^{K}(p_i - e_i)^2 \quad (7)$$

where K is the number of data, p_i is the predicted value and e_i is the experimental result. In the prediction of a parameter, different input variables (predictors) are contributing to define the behavior of target component as it depends on various affecting factors. By increasing the number of affecting factors, the relative contribution of predictive variables is characterized unclearly in predictive model. To overcome this problem, the different input variables can be ranked in terms of their potential influence on target value. This method determines those input variables that should be focused on to improve the efficiency of the process (Santos et al., 2019) . In this regards, relative importance is an index to specify the effect of different input variables on prediction of output parameter. The relative effects of independent variables (R_{Cl_2}, R, etc.) on dependent variables (R_{RCS}, $R_{HO\cdot}$) based on weighted coefficients can be derived using Eq. (8).

$$E_j = \frac{\sum_{t=1}^{t=N_h}\left(\left(|W_{jt}^{ih}|/\sum_{k=1}^{k=N_i}|W_{kt}^{ih}|\right)\times|W_{tn}^{ho}|\right)}{\sum_{k=1}^{N_i}\left\{\Sigma_{t=1}^{t=N_h}\left(\left(|W_{jt}^{ih}|/\Sigma_{k=1}^{N_i}|W_{kt}^{ih}|\right)\times|W_{tn}^{ho}|\right)\right\}} \quad (8)$$

where E_j, W and N are the relative importance of the jth input variable on R_{RCS}, weighted coefficient, and the number of neurons, respectively. The subscripts 'k', 't' and 'n' refer to input, hidden and output neurons, respectively and the superscripts 'i', 'h' and 'o' refer to input, hidden and output layers, respectively (Kıranşan et al., 2015).

Furthermore, deciding on the best values for ANN hyperparameters is one of the most challenging tasks in model generation. In this regard, an optimization method was implemented in this study to find the best possible values for the size of the hidden layer and learning rate based on an objective function model containing two optimizable variables. Accordingly, the objective function was optimized through 30 iterations of training process with different random values of hidden layer size and learning rate and finally the optimum combination of variables was used to construct the ANN model.

3. Results and discussion

3.1. Degradation kinetics

Fig. 5A illustrates the degradation of TMP with respect to time via direct UV photolysis at 254 nm, dark chlorination and UV(254)/Cl_2 at both pH 7 and 8. For direct UV photolysis, there were negligible changes in TMP concentration of about 3% observed. In Table S2, TMP's molar absorption coefficient (ε_{TMP}) is 2942 $M^{-1}cm^{-1}$ (Baeza and Knappe, 2011) and peaks up to 3650 (±50) $M^{-1}cm^{-1}$ (Wu et al., 2016). Having a high ε_{TMP} indicates that a compound is photo-labile. TMP, however, has a low quantum yield (Φ_{TMP}) of 1.18 (±0.11) × 10^{-3} (Baeza and Knappe, 2011). Therefore, this gives TMP its photo-stability and attributes to its low decay rate due to UV irradiation alone. Plots remained linear for both chlorination and chlorine photolysis, ascertaining a pseudo first-order kinetics model. The pseudo first-order rate constants (*k'*) were 2.78 (±0.25) × 10^{-3} s^{-1}, 1.44 (±0.19) × 10^{-3} s^{-1} for dark chlorination at pH 7 and 8, and 1.56 (±0.10) × 10^{-2} s^{-1} and 1.42 (±0.15) × 10^{-2} s^{-1} for UV/Cl_2 at pH 7 and 8 (Fig. 5B). Dark chlorination at pH 7 achieved a 2 log TMP removal within

Table 2
$k_{f,\lambda}'$ of TMP degradation by UV/Cl_2 system at various pHs and wavelengths.

pH ^{Kf}	$k_{f,254}'$ (cm^2mJ^{-1})	$k_{f,265}'$(cm^2mJ^{-1})	$k_{f,275}'$(cm^2mJ^{-1})	$k_{f,310}'$(cm^2mJ^{-1})
pH 6	0.0611	0.0305	0.0477	0.0106
pH 7	0.0649	0.0912	0.1275	0.0456
pH 8	0.0577	0.1743	0.2088	0.0874
pH 9	0.0424	0.2084	0.2747	0.1264

Table 3
Effect of chlorine dosage on k_f' of TMP degradation.

$[Cl_2]$ (mg/L)	$k_{f,265}'$ (cm^2mJ^{-1})	$k_{f,275}'$(cm^2mJ^{-1})	$k_{f,310}'$(cm^2mJ^{-1})
0.3	0.0023	0.008	0.0064
1	0.0576	0.06475	0.0286
3	0.17433	0.2088	0.0874
4	0.17354	0.23268	0.15591
5	0.17275	0.25656	0.23242
6	0.17195	0.28045	0.30493

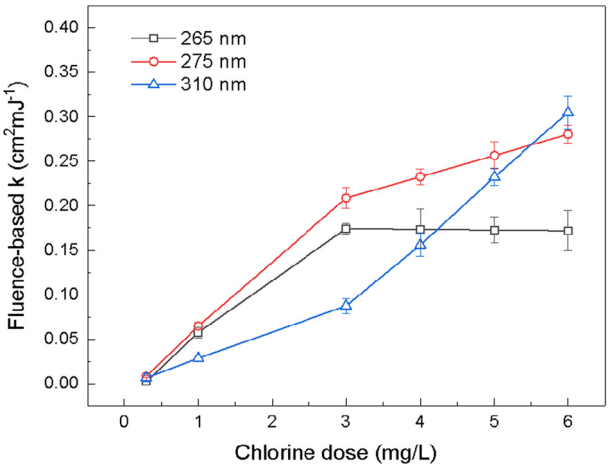

Fig. 8. Effect of chlorine dosage on k_f' of TMP degradation by UV/Cl_2 process at λ of 265, 275 and 310 nm. Condition: $[TMP]_0$ = 0.6889 μM (0.2 mg/L), $[Cl_2]_0$ = 4.225, 14.08, 42.25-84.51 μM (0.3, 1, 3-6 mg/L), pH 8.

30 minutes, whilst chlorine photolysis took 5 minutes. Chlorine photolysis greatly improved the degradation rate of TMP by 44.3% and 119% compared to dark chlorination at pH 7 and 8, respectively. Similarly, the k' values for UV/Cl_2 process were 5.61 and 9.86 times higher than that of dark chlorination at pH 7 and 8, respectively. This can be attributed to the formation of reactive oxidant species such as $Cl^{\bullet}$, $Cl_2^{-\bullet}$, $ClO^{\bullet}$ and $HO^{\bullet}$ from chlorine photolysis (Fang et al., 2014; Wu et al., 2016; Xiang et al., 2016).

3.1.1. Effect of pH

Fig. 6 compares the performances of the dark chlorination process at pH 6, 7, 8 and 9. The pseudo first-order rate constants of TMP reacting with free chlorine generally followed a descending order of magnitude with the exception of pH 6: 2.78 (±0.25) × 10^{-3} s^{-1} (pH 7), 1.44 (±0.19) × 10^{-3} s^{-1} (pH 8), 1.1 (±0.1) × 10^{-3} s^{-1} (pH 6) and 6.0 (±0.6) × 10^{-4} s^{-1} (pH 9). The variations in k' and removal rates with pH are due to the pH-dependent dissociations of TMP. In Fig. S5, TMP is a tri-protic acid across the pH range of 1-14, with two pK_as - namely $pK_{a,\ 1}(TMP^{++}/TMP^{+})$ = 3.2 and $pK_{a,\ 2}(TMP^{+}/TMP)$ = 7.1. According to Dodd and Huang (2007), the rate constant of TMP with HOCl was 160$M^{-1}S^{-1}$, while the rate constant of TMP^+ with HOCl was 6.2$M^{-1}S^{-1}$. Since pH 7 is closer to $pK_{a,\ 2}$ = 7.1, there exists more TMP than TMP^+ in the testing solution at pH 7 compared to pH 6. Thus, dark chlorination occurred faster at pH 7 than 6.

Table 4
Normalised R_{RCS}' at different wavelengths and pH in UV/Cl_2 system.

pH ^{Rrcs}	$R_{RCS,\ 254}'$	$R_{RCS,\ 265}'$	$R_{RCS,\ 275}'$	$R_{RCS,\ 310}'$
pH 6	67.90565	72.41922	76.87677	8.255017
pH 7	70.43572	72.99329	86.31932	18.48363
pH 8	78.79018	91.51267	89.07738	52.66731
pH 9	75.37535	77.69417	79.06214	48.07064

As for the UV/Cl_2 process, there was good agreement that employment of chlorine photolysis at 254 nm in acidic mediums tended to achieve high efficiency and efficacy than in alkaline mediums due to higher quantum yields and lower radical quenching rates (Fang et al., 2014; Qin et al., 2014). In Fig. 7B, the fluence based rate constants for the UV/Cl_2 process at 254 nm (k_f') at pH 6 to 9 were 0.0611 $mJ^{-1}cm^2$, 0.0649 $mJ^{-1}cm^2$, 0.0577 $mJ^{-1}cm^2$ and 0.04243 $mJ^{-1}cm^2$, respectively. The rate of chlorine photolysis is a non-factor in this case because at λ = 254 specifically, both HOCl and OCl^- have approximately the same ε ($\varepsilon_{UV/HOCl,\ 254}$ = $\varepsilon_{UV/OCl-,\ 254}$ ≈ 59~66 $M^{-1}cm^{-1}$) (Feng et al., 2007; Zhao et al., 2009) and thus the rate of chlorine photolysis would be the same irrespective of pH. Both HOCl and OCl^- contribute to radical scavenging and the rate constants of radical scavenging of $HO^{\bullet}$ and $Cl^{\bullet}$ by OCl^- were 4.9 and 2.7 times faster than that by HOCl, respectively (Table S1, Eqs. (R10)–(11), (13)–(14)). Since the dominant chlorine species would be OCl^- at alkaline conditions, scavenging of $HO^{\bullet}$ and $Cl^{\bullet}$ would be faster.

$ClO^{\bullet}$ is generated as a result of radical scavenging of $HO^{\bullet}$ and $Cl^{\bullet}$ and $ClO^{\bullet}$ demethylates the trimethoxybenzyl moiety of TMP (Alfassi et al., 1988) - also known as 3,4,5-Trimethoxytoluene (TMT). More $ClO^{\bullet}$ is generated at alkaline conditions since radical scavenging of $HO^{\bullet}$ and $Cl^{\bullet}$ by OCl^- is faster than that by HOCl. In the radicals' reaction with TMT (Eqs. (9)–(12)), $Cl^{\bullet}$ reacted with TMT the fastest (NIST, 2002), followed by $HO^{\bullet}$ (Luo et al., 2012) and then $ClO^{\bullet}$ (Alfassi et al., 1988). The $k_{f,\ 254}'$ obtained is congruent with literature that UV(254)/Cl_2 systems are more effective at acidic conditions because slower radical scavenging at acidic conditions by HOCl results in more $HO^{\bullet}$ and $Cl^{\bullet}$ and less $ClO^{\bullet}$ generated to react with TMT, as compared to alkaline conditions.

$$Cl^{\bullet} + TMT \xrightarrow{k_{Cl^{\bullet}/TMT}} \text{products},\ k_{Cl^{\bullet}/TMT} = 1.9 \times 10^{10}\ M^{-1}S^{-1} \quad (9)$$

$$HO^{\bullet} + TMT \xrightarrow{k_{HO^{\bullet}/TMT}} \text{products},\ k_{HO^{\bullet}/TMT} = 8.1 \times 10^{9}\ M^{-1}S^{-1} \quad (10)$$

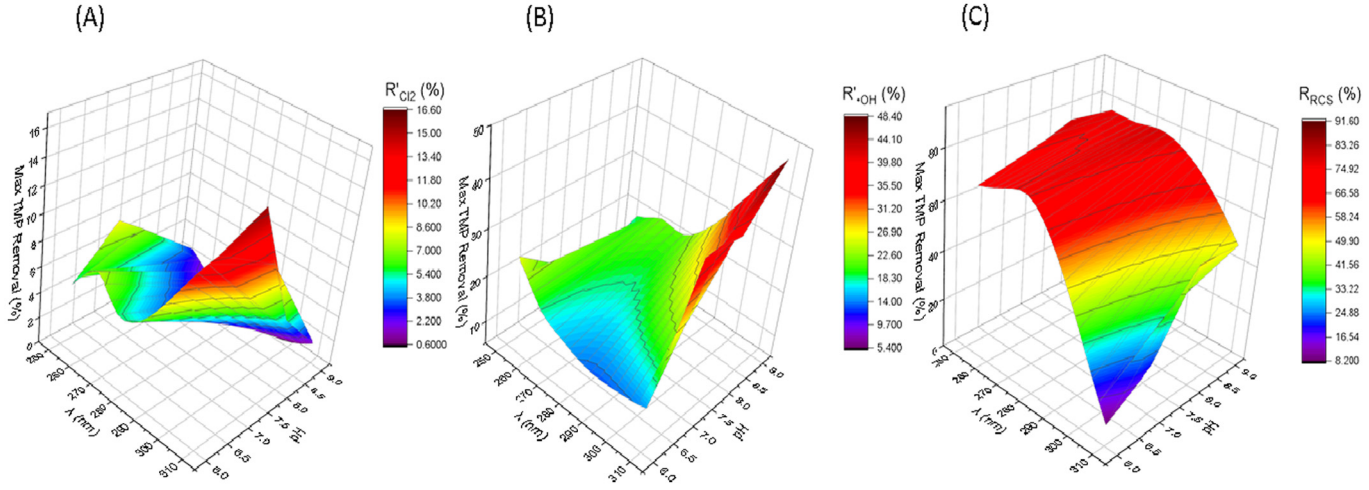

Fig. 9. (A): TMP removal efficiency by chlorine (R_{Cl_2}'), (B): TMP removal efficiency by $HO^{\bullet}$ ($R_{HO^{\bullet}}'$), (C): TMP removal efficiency by RCS (R_{RCS}'). Conditions: $[TMP]_0$ = 0.6889 μM (0.2 mg/L), $[Cl_2]_0$ = 42.25 μM (3 mg/L), pH 6-9, $[NB]_0$ = 0.8122 μM (0.1 mg/L).

Table 5
The performance of the generated models with different hidden layer sizes and learning rates through 30 iterations.

Iteration	Evaluation result	Hidden layer size	Objective learning rates	Objective function	Objective runtime (s)	Best so far (Observed)	Best so far (Estimated)
1	Best	10	0.014832	0.33973	4.2997	0.33973	0.33973
2	Accept	10	0.089718	0.34536	1.7747	0.33973	0.34032
3	Accept	16	0.042554	0.34763	4.6004	0.33973	0.33973
4	Accept	18	0.010618	0.34353	4.2072	0.33973	0.33973
5	Accept	5	0.015504	0.34037	0.56291	0.33973	0.33973
6	Accept	6	0.013609	0.34031	0.92159	0.33973	0.33998
7	Accept	18	0.014522	0.35032	2.1109	0.33973	0.34117
8	Accept	8	0.012247	0.34144	0.97211	0.33973	0.33973
9	Accept	8	0.015523	0.34369	0.53046	0.33973	0.34167
10	Accept	5	0.010177	0.341	0.30368	0.33973	0.34141
11	Accept	4	0.010013	0.33983	1.3951	0.33973	0.3411
12	Accept	1	0.010008	0.34922	0.41861	0.33973	0.34105
13	Accept	5	0.011192	0.34142	0.30384	0.33973	0.33973
14	Accept	10	0.01244	0.34191	1.2803	0.33973	0.33973
15	Accept	11	0.016051	0.34509	1.3119	0.33973	0.34111
16	Accept	6	0.01002	0.34239	0.28338	0.33973	0.3412
17	Best	5	0.017224	0.33935	0.28995	0.33935	0.34069
18	Best	5	0.022048	0.33809	0.3848	0.33809	0.34009
19	Accept	5	0.028835	0.33921	0.29264	0.33809	.33982
20	Accept	5	0.031543	0.33931	0.2615	0.33809	0.33943
21	Accept	5	0.029136	0.34066	0.2828	0.33809	0.33965
22	Accept	4	0.026181	0.34114	0.23955	0.33809	0.33979
23	Accept	1	0.099854	0.35004	0.22939	0.33809	0.34001
24	Accept	5	0.099794	0.3416	0.43122	0.33809	0.34005
25	Accept	14	0.010049	0.35059	3.1453	0.33809	0.34005
26	Accept	20	0.010012	0.33912	1.7434	0.33809	0.34007
27	Accept	20	0.010039	0.34342	2.3146	0.33809	0.34022
28	Best	3	0.01001	.33725	0.18883	0.33725	0.34023
29	Accept	4	0.010017	0.34007	0.30641	0.33725	0.3402
30	Best	3	0.01011	0.33662	0.19248	0.33662	0.33808

$$ClO^{\bullet} + TMT \xrightarrow{k_{ClO^{\bullet}/TMT}} \text{products}, k_{ClO^{\bullet}/TMT} = 2.1 \times 10^{9}\ M^{-1}S^{-1} \quad (11)$$

$$Cl_2^{-\bullet} + TMT \xrightarrow{k_{Cl_2^{-\bullet}/TMT}} \text{products}, k_{Cl_2^{-\bullet}/TMT} = 2.0 \times 10^{8}\ M^{-1}S^{-1} \quad (12)$$

3.1.2. Effect of wavelength

UV-LEDs at λ of 265, 275 and 310nm were applied for chlorine photolysis experiments. Fluence-based pseudo first-order rate constant k_f' were used instead of time-based rate constant k' because the four UV devices have different UV fluence rates identified earlier in Table S3 and the corresponding k_f' are listed in Table 2. Fig. 7A shows that k_f' had an upward trend as pH was increased - deviating from the trend observed at 254 nm. Yin et al. (2018) propounded that the wavelength dependency of chlorine photolysis on its molar absorption coefficients were higher at alkaline pHs - indicating that (free) chlorine photo decay rates were more dependent on their molar absorption coefficients (ε) than their quantum yields (Φ). Since OCl^- has a higher molar absorption coefficient compared to HOCl at

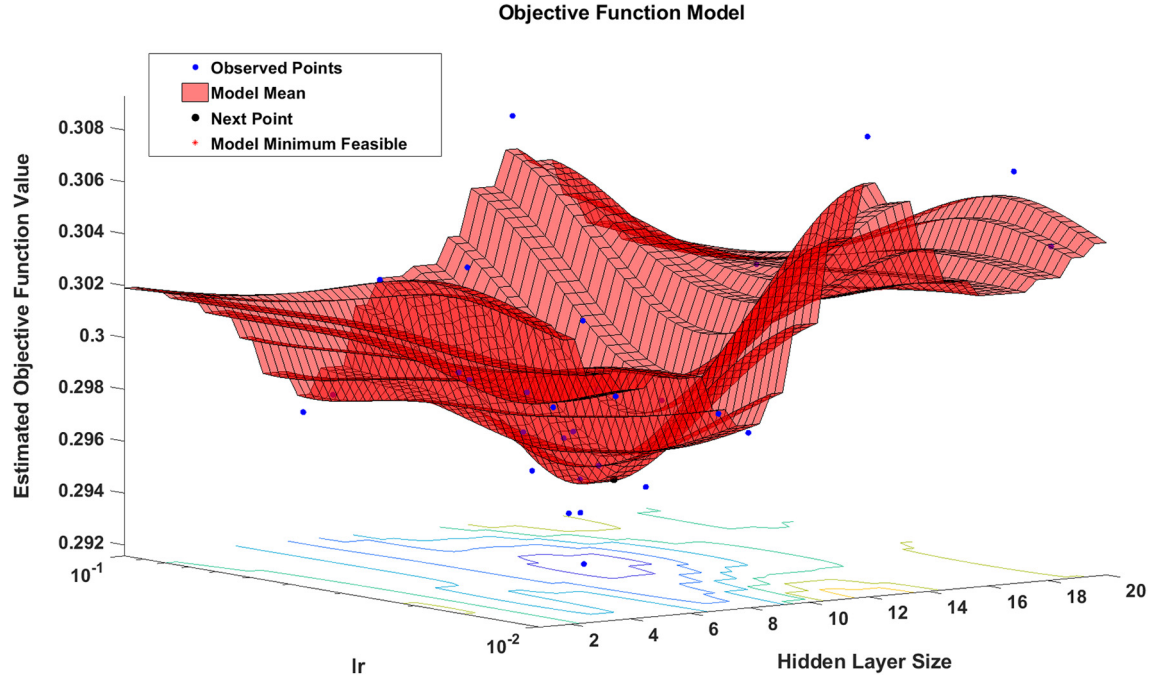

Fig. 10. The graphical illustration of the best possible solution in optimizing the objective function.

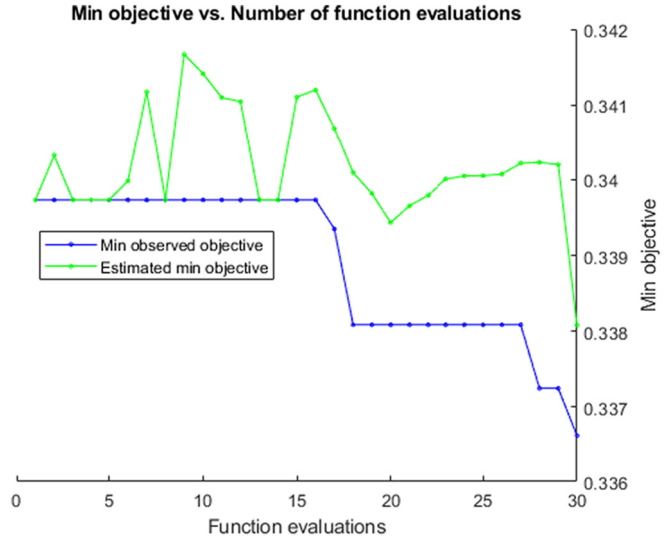

Fig. 11. The progression of optimization process during 30 iterations to obtain the absolute minimum of objective function.

higher wavelengths (Fig. S3), there is increased propensity for more RCS formation and contribution in alkaline chlorine photolysis for TMP removals. This results in more $Cl^{\bullet}$, $Cl_2^{-\bullet}$ and $ClO^{\bullet}$ generated (Table S1, Eqs. (R2), (R13)-(R22)) to react with TMP (Eqs. (10)–(12)).

At alkaline mediums of pH 8 and 9, the performances of UV-LED/Cl_2 systems followed the following trend: UV(275)/Cl_2 > UV(265)/Cl_2 > UV(310)/Cl_2 > UV(254)/Cl_2 (Fig. 7A-B). Following the observed trend - changing the wavelengths improved k_f' by 362%, 302%, 151% at pH 8 and 648%, 492% and 298% at pH 9 by using $k_{f,\,254}'$ as a basis of comparison. Collectively, the UV-LED 275 systems triumphed all other UV systems in the application of chlorine photolysis of TMP at alkaline pHs. The k_f' trend obtained is not congruent with Yin et al.'s hypothesis (Yin et al., 2018) If chlorine photo decay rates were extremely dependent on their molar absorption coefficients (ε), the performance of chlorine photolysis would have been: UV(310)/Cl_2 > UV(275)/Cl_2 > UV(265)/Cl_2 > UV(254)/Cl_2 because $\varepsilon_{OCl,\,310} > \varepsilon_{OCl,\,275} > \varepsilon_{OCl,\,265} > \varepsilon_{OCl,\,254}$ (Fig. S3). This implies that chlorine photolysis could have a higher dependency on not only molar absorptivity, but also its quantum yields at higher pH. The trend in quantum yields of OCl^- across different wavelengths ($\Phi_{OCl,\,\lambda}$) is the polar opposite to its molar absorption coefficient: $\Phi_{OCl,\,254} = 1.058 > \Phi_{OCl,\,265} = 0.995 > \Phi_{OCl,\,275} = 0.937 > \Phi_{OCl,\,310} = 0.737$ (Yin et al., 2018). Although OCl^- at 275 nm does not have the highest molar absorption coefficient (as compared to 310 nm) nor does it have the highest quantum yield to decompose the most OCl^- to form radical chlorine species upon UV irradiation (as compared to 254 nm), the UV(275)/Cl_2 systems provide a sweet spot for OCl^- to have the best of both worlds. Results are in accordance with Wang et al.'s application of UV-LED in chlorine photolysis of carbamazepine and Kwon et al.'s usage of UV-275 LEDs to remove nitrobenzene and ibuprofen (Kwon et al., 2018; Wang et al., 2017).

Table 6
The performance of each generated ANN model on their corresponding data fold including MSE and correlation coefficient.

Fold number	Number of data in training set	Number of data in test set	Correlation coefficient (Training)	MSE (Training)	Correlation coefficient (Test)	MSE (Test)
1	86	6	0.9991	6.94E-05	0.9994	2.77E-05
2	85	7	0.9986	1.00E-04	0.9944	6.01E-04
3	85	7	0.9988	9.40E-05	0.9908	7.79E-04
4	86	6	0.9995	3.76E-05	0.9991	1.10E-04
5	86	6	0.9999	7.09E-06	0.9992	5.87E-05
6	86	6	0.9994	4.86E-05	0.9705	1.94E-03
7	86	6	0.9999	1.02E-05	0.9979	1.21E-04
8	86	6	0.9997	2.37E-05	0.9951	2.87E-04
9	86	6	0.9983	1.23E-04	0.9970	3.24E-04
10	86	6	0.9994	4.37E-05	0.9996	3.72E-05
11	86	6	0.9977	1.81E-04	0.9622	2.62E-03
12	86	6	0.9995	3.71E-05	0.9953	3.88E-04
13	86	6	0.9997	2.64E-05	0.9881	6.41E-04
14	86	6	0.9991	6.47E-05	0.9988	1.23E-04
15	86	6	0.9994	4.59E-05	0.9993	3.29E-05
Average	86	6	0.9992	6.08E-05	0.992447	5.39E-04

3.1.3. Effect of chlorine dosage

Both Table 3 and Fig. 8 show the $k_{f,\,\lambda}'$ of TMP degradation at pH 8 by employing UV/Cl_2 systems with wavelengths of 265, 275 and 310 nm, respectively. As chlorine dosage was increased from 4.23 to 42.3 μM (0.3-3 mg/L), higher chlorine concentrations brought about an increased formation of reactive oxidant species such as $Cl^{\bullet}$, $Cl_2^{-\bullet}$, $ClO^{\bullet}$ and $HO^{\bullet}$ from chlorine photolysis. As a result, $k_{f,\,\lambda}'$ was increased linearly by 74.8, 25.1 and 12.7 times for 265, 275 and 310 nm UV/Cl_2 systems, respectively. However, dosing chlorine beyond 42.25 μM resulted in different trends for the 3 UV-LED/Cl_2 systems. $k_{f,\,265}'$ seemed to reach a limit of 0.0172 cm^2mJ^{-1} and plateaued. $k_{f,\,275}'$ was increased at a slower rate as compared with dosing chlorine within a range of 4.23 to 42.3 μM. $k_{f,\,310}'$, however, seemed to deviate from the 265 and 275 nm systems by increasing faster. This anomalous behavior depicted in $k_{f,\,310}'$ could perhaps be attributed to photolyzing OCl^- at close to λ of 320 nm. The photolysis of OCl^- at λ < 320 nm generates products like $O^{-\bullet}$ and $Cl^{\bullet}$ (Table S1, Eq. (R2)) or excited single state oxygen atoms $O(^1D)$ and Cl^- (Table S1, Eq. (R3)). The conjugate base of $HO^{\bullet}$ is $O^{-\bullet}$ and can react quickly with hydrogen ions to reform $HO^{\bullet}$ (Table S1, Eq. (R6)) whilst $O(^1D)$ can produce $HO^{\bullet}$ after reacting with water (Table S1, Eq. (R7)). At λ > 320 nm, OCl^- produces ground state oxygen atoms $O(^3P)$ and Cl^- (Table S1, Eq. (R4)). $O(^3P)$ can react with oxygen to form ozone (Table S1, Eq. (R8)). Ozone generation has received minimal attention in literature because it is only favoured when higher wavelengths of light are used. The further generation of both $HO^{\bullet}$ and ozone brought about by higher chlorine dosages accelerates trimethoprim degradation when applied at λ close to 320 nm.

3.2. Role of reactive species

Chlorine photolysis produces several oxidant species once chlorine is subjected to UV irradiation. To quantify the varying contributions brought about by the multifarious reactive species present in the system, characterisation of UV/Cl_2 process with available kinetic data is necessary (Eq. (S1)). To prevent overcomplication of the general kinetic model established in Eq (S1) to compare the UV/Cl_2 systems across different wavelengths, several assumptions were made:

Firstly, elucidating the exact rate constants and concentrations by each RCS in UV/Cl_2 systems is complex because the system produces multifarious reactive oxidant species and as a result, the degradation of any compound by the reactants are multifaceted and simultaneous. Since rate constants of specific RCS - namely $Cl^{\bullet}$, $Cl_2^{-\bullet}$ and $ClO^{\bullet}$ with most pollutants are unavailable, the synonymous contributions of RCS to TMP degradation will be simplified to Eq. (S2). The kinetic equation is further simplified to Eq. (S3) due to TMP's photostability. Normalising Eq. (S3) by dividing the equation with $[TMP]_o = 0.6889$ μM gives us Eq. (S4) - which will be referred to throughout this section as:

$$R' = R'_{Cl_2} + R'_{HO^{\bullet}} + R'_{RCS} \quad (13)$$

where R′, R_{Cl_2}', $R_{HO^{\bullet}}'$, R_{RCS}' are the normalised overall removal efficiency of TMP at time t, normalised removal efficiency of TMP by chlorine, $HO^{\bullet}$ radicals and reactive chlorine species, respectively. To elucidate the concentration of $HO^{\bullet}$ to calculate $R_{HO^{\bullet}}'$, nitrobenzene (NB) was used as an $HO^{\bullet}$ probe because not only is it unamenable to chlorination and UV photolysis, it also has extremely low reaction rates with other oxidants generated in UV/Cl_2 system (Fang et al., 2014; Watts and Linden, 2007; Xiang et al., 2016). RCS contributions can be calculated by subtracting chlorine (Eq. (S5))

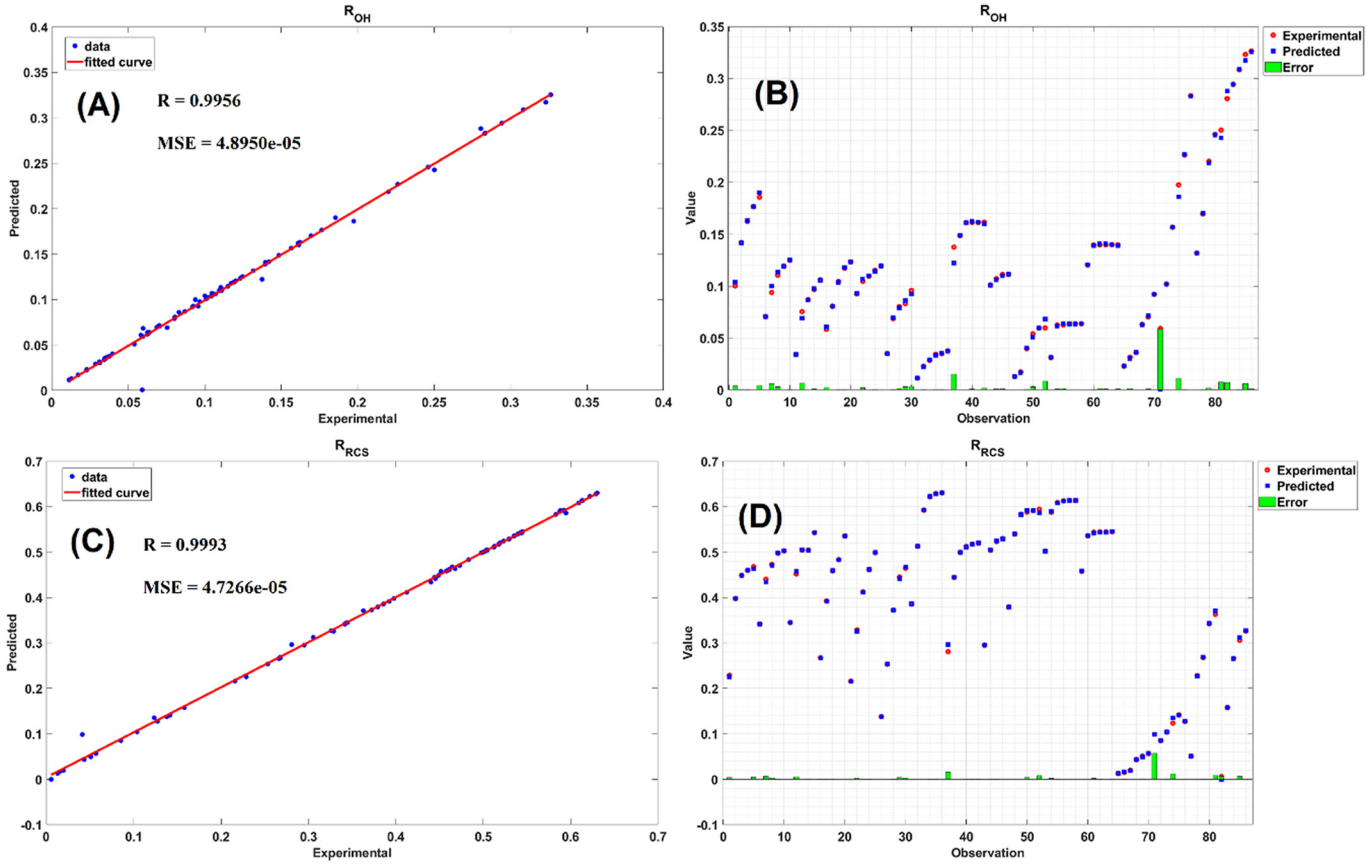

Fig. 12. Scatter plots of training datasets for (A), (B): predicted and experimental $R_{HO^{\bullet}}$ with corresponding correlation coefficient, (C), (D): predicted and experimental R_{RCS} with corresponding correlation coefficient.

and $HO^{\bullet}$ contributions (Eqs. (S6)–(S11)) from the overall TMP removal (Eq. (S12)). The full details of the derivation can be found in Text S3. TMP removals attributed by various oxidants present in the UV/Cl_2 system are presented in Figs. S7-S10.

Secondly, the formation of hypochlorous radical anion ($HOCl^{-\bullet}$) via $Cl^{\bullet}$ (Table S1, Eq. (R16)) was not considered as part of the RCS in this study. By virtue of reaction rate constants, $Cl^{\bullet}$ would react preferentially with the 3,4,5-Trimethoxytoluene (TMT) portion of TMP at 10^{10} $M^{-1}S^{-1}$ (Eq. (9)) instead of forming $HOCl^{-\bullet}$ via water at 10^{2} to 10^{4} $M^{-1}S^{-1}$ (Table S1, Eq. (R16)). Thus, there will not be any depletion $Cl^{\bullet}$ to form $HOCl^{-\bullet}$, which in turn would not affect R_{RCS}' (normalised removal efficiency of TMP by reactive chlorine species). Moreover, there will be no subsequent formation of $HO^{\bullet}$ due to dissociation of $HOCl^{-\bullet}$ (Table S1, Eq. (R20)), no formation of $Cl_2^{-\bullet}$ due to $HOCl^{-\bullet}$ reaction with chloride ions (Table S1, Eq. (R21)) and no reformation of $Cl^{\bullet}$ due to $HOCl^{-\bullet}$ reaction with hydrogen ions (Table S1, Eq. (R22)).

Lastly, section 3.1.3 postulates that chlorine photolysis at wavelengths close to 320 nm will generate both $HO^{\bullet}$ and ozone to accelerate trimethoprim degradation. Since the irradiation wavelength is 310nm, the main contributor of increased radicals in UV(310)/Cl_2 systems is not ozone, but rather, $HO^{\bullet}$. The photolysis of OCl^{-} at $\lambda < 320$ nm generates products like $O^{-\bullet}$ and $Cl^{\bullet}$ (Table S1, Eq. (R2)) or excited single state oxygen atoms $O(^1D)$ and Cl^{-} (Table S1, Eq. (R3)). The conjugate base of $HO^{\bullet}$ is $O^{-\bullet}$ and can react quickly with hydrogen ions to form $HO^{\bullet}$ (Table S1, Eq. (R6)) whilst $O(^1D)$ can produce $HO^{\bullet}$ after reacting with water (Table S1, Eq. (R7)). The quantum yields of $O(^1D)$ is 0.133 mol/Es (McGrath and McGarvey, 1967), and that leads to the formation of $HO^{\bullet}$ at a rate of 1.2 x 10^{11} $M^{-1}S^{-1}$ (Table S1, Eq. (R7)). On the other hand, the photolysis of OCl^{-} at $\lambda > 320$ nm generates $O(^3P)$. The quantum yield of $O(^3P)$ at 0.074 mol/Es (Buxton and Subhani, 1972; Kläning et al., 1984; Treinin, n.d.) and that encourages the formation of ozone at a rate of 4 x 10^{9} $M^{-1}S^{-1}$ (Table S1, Eq. (R8)). Since both quantum yields and reaction rate constants favour the formation of $HO^{\bullet}$, we shall presume that the main contributor of increased radicals in UV(310)/Cl_2 systems is not ozone, but rather, $HO^{\bullet}$.

In Fig. 9A, it can be seen that R_{Cl_2}' peaked across pH 7 across all UV/Cl_2 systems. As pH was increased from 6 to 7, R_{Cl_2}' was increased from 4.62% to 8.49%, 8.58% to 10.1%, 4.72% to 4.86% and 13.8% to 16.6%, for UV (254)/Cl_2, UV(265)/Cl_2, UV(275)/Cl_2 and UV(310)/Cl_2 systems, respectively. The reason was previously elaborated in sections 3.1.1. At pH 7, there exists more TMP than TMP^{+} ($pK_{a,\ 2}((TMP^{+}/TMP)) = 7.1$). TMP reacts with HOCl at 160$M^{-1}S^{-1}$, compared to TMP^{+} with HOCl at 6.2$M^{-1}S^{-1}$. Therefore, R_{Cl_2}'would increase as pH was increased from 6 to 7. RCS played a pivotal role in TMP degradation at all pHs and wavelengths. From Table 4 and Fig. 9C, R_{RCS}' was increased from 67% to 76%, 70% to 86%, 78% to 91% and 75% to 79% as wavelength was increased from 254 to 275 nm at pH 6-9, respectively. Interestingly, R_{RCS}' was decreased from 76% to 8%, 86% to 18%, 91% to 52% and 79% to 48% as wavelength approaches UV-B ($\lambda = 310$ nm) region at pH 6-9, respectively. This decline in R_{RCS}' at $\lambda = 310$ nm was compensated by an increase in R_{HO}' in pH 7-9 (Fig. S10A–D). At pH 7-9, R_{HO}' was the highest ranging from 36% to 48% in UV (310)/Cl_2 system as compared to 5% to 23% in UV (254, 265, 275)/Cl_2 systems. The compensation of RCS by $HO^{\bullet}$ can also be observed from a pH increment angle - R_{RCS}' peaked at pH 8 at 78%, 91%, 89% and 52% before declining to 77%, 75%, 79% and 48% at pH 9 for 254, 265, 275 and 310 nm respectively (Fig. 9A–C). When pH was 9, the decline in R_{RCS}' was compensated by an increase in R_{HO}' in all UV/Cl_2 systems. R_{HO}' also tended to be the highest at pH 9 except for UV (254)/Cl_2 systems. The reason attributed for such increase in R_{HO}' in UV (310)/Cl_2 system is because photolysis of OCl^{-} generates products like $O(^1D)$ (Table S1, Eq. (R3)), which reacts with water to form $HO^{\bullet}$ (Table S1, Eq. (R7)). This increased the available $HO^{\bullet}$ in the system and resulted in increased R_{HO}' at pH 9.

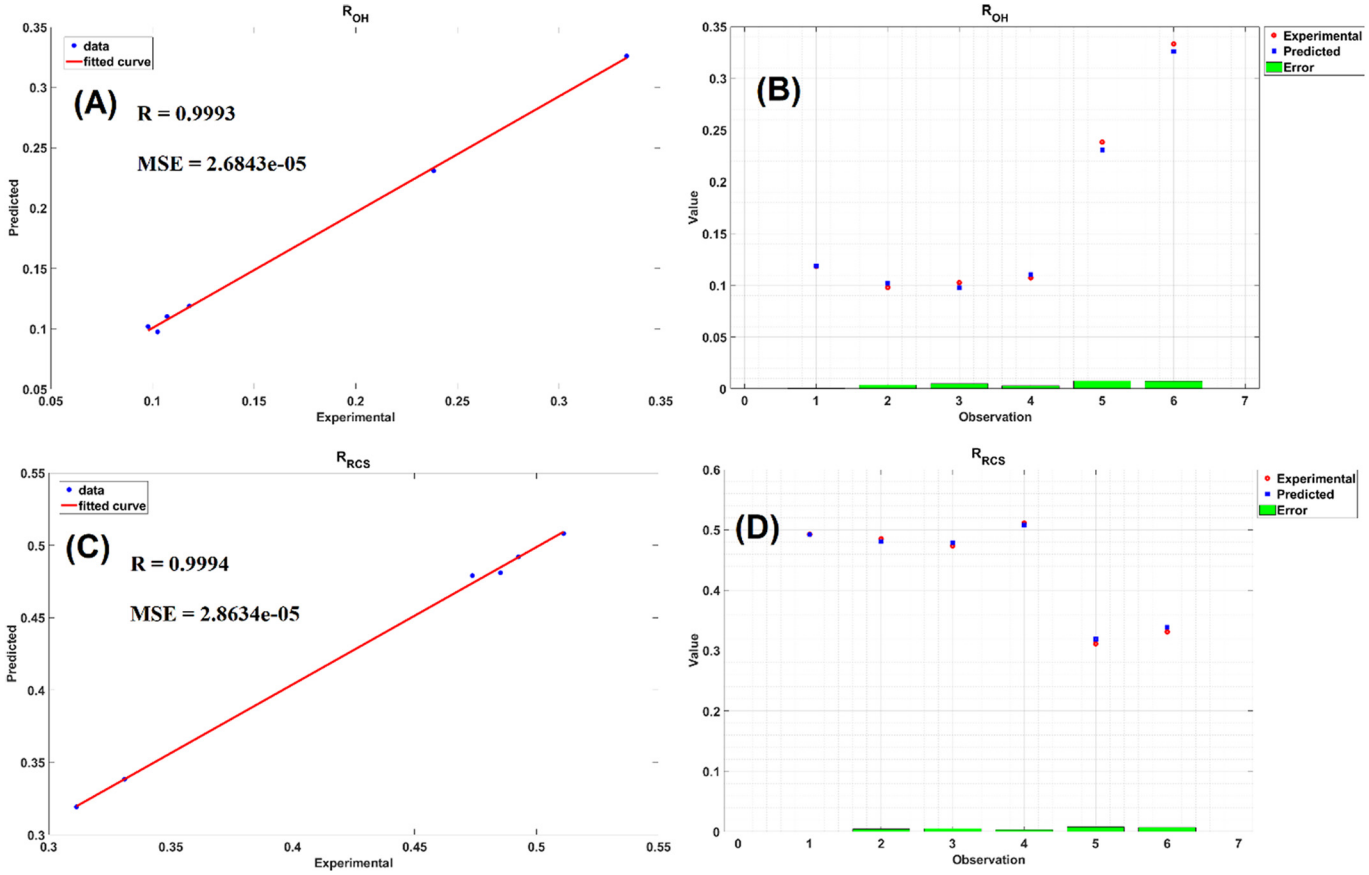

Fig. 13. Scatter plots of test dataset for (A), (B): predicted and experimental $R_{HO^{\cdot}}$ with corresponding correlation coefficient, (C), (D): predicted and experimental R_{RCS} with corresponding correlation coefficient.

3.3. Prediction of $R_{HO^{\cdot}}$ and RCS contribution

The contribution brought about by RCS could possibly be underestimated or flawed because unnormalized removal efficiencies by RCS on TMP are assumed to be the subtraction of removal efficiencies by chlorine and $HO^{\bullet}$ from the total removal efficiency of TMP (Eq. (S12)). Eq. (S12) dismisses the possibility that RCS could play a much bigger role than expected. Moreover, the estimation of TMP removal contributed by $HO^{\bullet}$ is a tedious experimental process, there will be tangible benefits in applying ANN to predict the contribution of $HO^{\bullet}$ in the UV/Cl_2 systems.

ANN was then applied to model experimental results, predict subsequent removal efficiencies, and ascertain the congruency between the experimentally determined $R_{HO^{\cdot}}$ and R_{RCS} using Eq. (S2)–(S12) to those of $R_{HO^{\cdot}}$ and R_{RCS} predicted by ANN. As mentioned earlier, the optimum values for hidden layer size and learning rate was obtained based on an optimization objective function with two optimizable variables. It can be seen in Table 5 the performance of the generated models with different hidden layer sizes in the range of [1 20] and learning rates in the range of [0.01 0.1] was evaluated through 30 iterations. The best possible solution for this optimization problem was finally obtained where the objective function had an absolute minimum and the corresponding values for hidden layer size and learning rate were then used in ANN model generation (Fig. 10). The progression of optimization process during 30 iterations to obtain the absolute minimum of objective function is also provided in Fig. 11. Based on the results, a hidden layer with 10 neurons and a learning rate of 0.0346 were selected as the optimum values for generating the ANN model. To have a better generalization error, a 15-Fold cross validation step was implemented to examine the performance of the ANN model and the average correlation coefficient and MSE were obtained as 0.9992 and 6.0884e-05, respectively for training set and 5.3986e-04 and 0.9925, respectively for test set. Table 6 shows the performance of each generated ANN model on their corresponding data fold including MSE and correlation coefficient. Out of all generated ANN models on 15 folds of dataset, the best model in terms of its MSE value on test set was separated to show the best possible performance graphically and the results are shown in Fig. 12A-D for training set and Fig. 13A-D for test set. According to the results, the best model had correlation coefficients and MSE values of 0.9956 and 4.8950e-05, respectively on training set and 0.9993 and 2.6843e-05, respectively on test set for predicting $R_{HO^{\cdot}}$. Similarly, the correlation coefficients and MSE values for R_{RCS} prediction were obtained as 0.9993 and 4.7266e-05, respectively on training set and 0.9994 and 2.8634e-05, respectively on test set. The results showed high accuracy in predicting $R_{HO^{\cdot}}$ and R_{RCS} roles on TMP degradation using ANN model except in a few observations (i.e observation 71) in the training set which might be due to the possible errors in experimental measurements and hence changing the properties of these few records of data from other available records. Therefore, observation 71can be considered as an outlier.

Furthermore, The obtained results showed that the relative importance of exposure time, λ, overall rate (R), R_{Cl_2}, and pH in prediction of $R_{HO^{\cdot}}$ and R_{RCS} roles on TMP degradation was 46.43%, 18.26%, 14.05%, 12.49%, and 8.78% for $R_{HO^{\cdot}}$ and 51.50%, 17.30%, 11.24%, 10.91%, and 9.04% for R_{RCS} in descending order, respectively (Table S5). By comparing the relative importance of independent variables in ANN model it can be concluded that exposure time had the most effect on prediction of $R_{HO^{\cdot}}$ and R_{RCS} among other affecting input variables. The longer the experimental time frame and exposure time UV light has on the entire UV/Cl_2 system, it increases the propensity of radical formation to remove TMP. The amount of free chlorine available (HOCl and OCl^{-}) decreases with exposure time, contributing to radical formation (Table S1, Eqs. (R1)–(R4)). Also, the increased exposure time allows for more scavenging of $HO^{\bullet}$ and $Cl^{\bullet}$ (Table S1,

Eqs. (R10)-(11), (13)-(14)), generating RCS like $ClO^{\bullet}$ which contributes to TMP degradation. On this basis, its concluded that ANN model constructed in this study is reliable as it is representing that the main component in defining the $R_{HO^{\bullet}}$ and R_{RCS} is exposure time with highest relative importance. Table of connection weights and biases is provided in Table S5.

4. Conclusion

This study investigated the use of the UV/Cl_2 system for breakdown of trimethoprim (TMP) across wider treatment conditions. By employing UV/Cl_2 in alkaline mediums and by changing the wavelengths via the use of UV-LEDs, its performance and applicability can be enhanced. In this study, TMP removals via chlorine photolysis followed the trend of UV (275)/Cl_2 > UV (265)/Cl_2 > UV (310)/Cl_2 > UV (254)/Cl_2. The results revealed that RCS played the most important role in TMP degradation and its contributions were increased with increasing pH and wavelength. $ClO^{\bullet}$ was generated as a result of radical scavenging and demethylating the trimethoxybenzyl moiety of TMP. However, the trend deviated when pH reached 9 and wavelength reached UV-B region. The involvement of RCS in TMP degradations in UV/Cl_2 systems at alkaline conditions could possibly be extrapolated to other PPCPs that contains aromatic moieties that are amendable to degradation by $ClO^{\bullet}$. As a result, $ClO^{\bullet}$ can compensate for the reduction of $HO^{\bullet}$ and $Cl^{\bullet}$ due to scavenging. In this study, chlorine photolysis employed in UV-B regions was found to have higher $HO^{\bullet}$ generation than UV-C chlorine photolysis plausibly due to $O(^1D)$ formation, which reacts with water to form $HO^{\bullet}$. An ANN model was applied on the datasets and the results showed that the model was able to predict $R_{HO^{\bullet}}$ and R_{RCS} accurately and the best topology was 5-10-2 with Bayesian Regularization as a training algorithm. Computing the relative importance of input variables in ANN models showed that exposure time had the most effect in prediction of $R_{HO^{\bullet}}$ and R_{RCS} confirming the accuracy and reliability of the model.

CRediT authorship contribution statement

Ying Shen Teo: Conceptualization, Investigation, Methodology, Writing – original draft. **Iman Jafari:** Investigation, Methodology, Software, Writing – original draft. **Fei Liang:** Investigation, Methodology. **Youmi Jung:** Conceptualization, Methodology. **Jan Peter Van der Hoek:** Writing – review & editing, Supervision. **Say Leong Ong:** Resources, Supervision. **Jiangyong Hu:** Funding acquisition, Resources, Supervision, Writing – review & editing.

Declaration of Competing Interest

The authors declare that they have no known competing financial interests or personal relationships that could have appeared to influence the work reported in this paper.

Acknowledgments

This work was supported by the Research Scholarship of the National University of Singapore and Singapore International Graduate Award (SINGA).

Appendix A. Supplementary data

Supplementary data to this article can be found online at https://doi.org/10.1016/j.scitotenv.2021.152551.

References

Alfassi, Z.B., Huie, R.E., Mosseri, S., Neta, P., 1988. Kinetics of one-electron oxidation by the ClO radical. Int. J. RadiatAppl. Instrum. Part C Radiat. Phys. Chem. 32, 85–88. https://doi.org/10.1016/1359-0197(88)90018-5.

APHA, AWWA, WEF, 1999. Standard Methods for the Examination of Water and Wastewater

Baeza, C., Knappe, D.R.U., 2011. Transformation kinetics of biochemically active compounds in low-pressure UV photolysis and UV/H2O2 advanced oxidation processes. Water Res. 45, 4531–4543. https://doi.org/10.1016/j.watres.2011.05.039.

Barakat, M.A., Tseng, J.M., Huang, C.P., 2005. Hydrogen peroxide-assisted photocatalytic oxidation of phenolic compounds. Appl. Catal. B Environ. 59, 99–104. https://doi.org/10.1016/j.apcatb.2005.01.004.

Batt, A.L., Kim, S., Aga, D.S., 2006. Enhanced biodegradation of iopromide and trimethoprim in nitrifying activated sludge. Environ. Sci. Technol. 40, 7367–7373. https://doi.org/10.1021/es060835v.

Ben, W., Sun, P., Huang, C.-H., 2016. Effects of combined UV and chlorine treatment on chloroform formation from triclosan. Chemosphere 150, 715–722. https://doi.org/10.1016/j.chemosphere.2015.12.071.

Bolton, J.R., Stefan, M.I., Shaw, P.-S., Lykke, K.R., 2011. Determination of the quantum yields of the potassium ferrioxalate and potassium iodide–iodate actinometers and a method for the calibration of radiometer detectors. J. Photochem. Photobiol. Chem. 222, 166–169. https://doi.org/10.1016/j.jphotochem.2011.05.017.

Buxton, G.V., Subhani, M.S., 1972. Radiation chemistry and photochemistry of oxychlorine ions. Part 2. —Photodecomposition of aqueous solutions of hypochlorite ions. J. Chem. Soc. Faraday Trans. 1 68, 958–969. https://doi.org/10.1039/F19726800958.

Carvajal, G., Roser, D.J., Sisson, S.A., Keegan, A., Khan, S.J., 2017. Bayesian belief network modelling of chlorine disinfection for human pathogenic viruses in municipal wastewater. Water Res. 109, 144–154. https://doi.org/10.1016/j.watres.2016.11.008.

Chan, P.Y., Gamal El-Din, M., Bolton, J.R., 2012. A solar-driven UV/Chlorine advanced oxidation process. Water Res. 46, 5672–5682. https://doi.org/10.1016/j.watres.2012.07.047.

Chen, J., Loeb, S., Kim, J.-H., 2017. LED revolution: fundamentals and prospects for UV disinfection applications. Environ. Sci. Water Res. Technol. 3, 188–202. https://doi.org/10.1039/C6EW00241B.

Chevremont, A.-C., Boudenne, J.-L., Coulomb, B., Farnet, A.-M., 2013a. Impact of watering with UV-LED-treated wastewater on microbial and physico-chemical parameters of soil. Water Res. 47, 1971–1982. https://doi.org/10.1016/j.watres.2013.01.006.

Chevremont, A.-C., Boudenne, J.-L., Coulomb, B., Farnet, A.-M., 2013b. Fate of carbamazepine and anthracene in soils watered with UV-LED treated wastewaters. Water Res. 47, 6574–6584. https://doi.org/10.1016/j.watres.2013.08.031.

Close, J., Ip, J., Lam, K.H., 2006. Water recycling with PV-powered UV-LED disinfection. Renew. Energy 31, 1657–1664. https://doi.org/10.1016/j.renene.2005.08.034.

Daughton, C.G., Ternes, T.A., 1999. Pharmaceuticals and personal care products in the environment: agents of subtle change? Environ. Health Perspect. 107, 907–938.

de Paula, F.C.C.R., de Pietro, A.C., Cass, Q.B., 2008. Simultaneous quantification of sulfamethoxazole and trimethoprim in whole egg samples by column-switching high-performance liquid chromatography using restricted access media column for on-line sample clean-up. J. Chromatogr. A 1189, 221–226. https://doi.org/10.1016/j.chroma.2007.08.046 31st International Symposium on High Performance Liquid Phase Separations and Related Techniques.

Dodd, M.C., Huang, C.-H., 2007. Aqueous chlorination of the antibacterial agent trimethoprim: reaction kinetics and pathways. Water Res. 41, 647–655. https://doi.org/10.1016/j.watres.2006.10.029.

Fang, J., Fu, Y., Shang, C., 2014. The roles of reactive species in micropollutant degradation in the UV/Free chlorine system. Environ. Sci. Technol. 48, 1859–1868. https://doi.org/10.1021/es4036094.

Feng, Y., Smith, D.W., Bolton, J.R., 2007. Photolysis of aqueous free chlorine species (HOCl and OCl–) with 254 nm ultraviolet light. J. Environ. Eng. Sci. 6, 277–284. https://doi.org/10.1139/s06-052.

Forsyth, J.E., Zhou, P., Mao, Q., Asato, S.S., Meschke, J.S., Dodd, M.C., 2013. Enhanced inactivation of Bacillus subtilis spores during solar photolysis of free available chlorine. Environ. Sci. Technol. 47, 12976–12984. https://doi.org/10.1021/es401906x.

Giwa, A., Daer, S., Ahmed, I., Marpu, P.R., Hasan, S.W., 2016. Experimental investigation and artificial neural networks ANNs modeling of electrically-enhanced membrane bioreactor for wastewater treatment. J. Water Process Eng. 11, 88–97. https://doi.org/10.1016/j.jwpe.2016.03.011.

Goldstein, S., Aschengrau, D., Diamant, Y., Rabani, J., 2007. Photolysis of aqueous H2O2: quantum yield and applications for polychromatic UV actinometry in photoreactors. Environ. Sci. Technol. 41, 7486–7490. https://doi.org/10.1021/es071379t.

Halling-Sørensen, B., Nors Nielsen, S., Lanzky, P.F., Ingerslev, F., Holten Lützhøft, H.C., Jørgensen, S.E., 1998. Occurrence, fate and effects of pharmaceutical substances in the environment- a review. Chemosphere 36, 357–393. https://doi.org/10.1016/S0045-6535(97)00354-8.

Hirsch, R., Ternes, T., Haberer, K., Kratz, K.-L., 1999. Occurrence of antibiotics in the aquatic environment. Sci. Total Environ. 225, 109–118. https://doi.org/10.1016/S0048-9697(98)00337-4.

Houtman, C.J., Kroesbergen, J., Lekkerkerker-Teunissen, K., van der Hoek, J.P., 2014. Human health risk assessment of the mixture of pharmaceuticals in dutch drinking water and its sources based on frequent monitoring data. Sci. Total Environ. 496, 54–62. https://doi.org/10.1016/j.scitotenv.2014.07.022.

Jelic, A., Gros, M., Ginebreda, A., Cespedes-Sánchez, R., Ventura, F., Petrovic, M., Barcelo, D., 2011. Occurrence, partition and removal of pharmaceuticals in sewage water and sludge during wastewater treatment. Water Res. 45, 1165–1176. https://doi.org/10.1016/j.watres.2010.11.010.

Jewell, K.S., Castronovo, S., Wick, A., Falås, P., Joss, A., Ternes, T.A., 2016. New insights into the transformation of trimethoprim during biological wastewater treatment. Water Res. 88, 550–557. https://doi.org/10.1016/j.watres.2015.10.026.

Jin, J., El-Din, M.G., Bolton, J.R., 2011. Assessment of the UV/Chlorine process as an advanced oxidation process. Water Res. 45, 1890–1896. https://doi.org/10.1016/j.watres.2010.12.008.

Karadurmuş, E., Taşkın, N., Göz, E., Yüceer, M., 2019. Prediction of bromate removal in drinking water using artificial neural networks. Ozone Sci. Eng. 41, 118–127. https://doi.org/10.1080/01919512.2018.1510763.

Kıranşan, M., Khataee, A., Karaca, S., Sheydaei, M., 2015. Artificial neural network modeling of photocatalytic removal of a disperse dye using synthesized of ZnO nanoparticles on montmorillonite. Spectrochim. Acta A Mol. Biomol. Spectrosc. 140, 465–473. https://doi.org/10.1016/j.saa.2014.12.100.

Kläning, U.K., Sehested, K., Wolff, T., 1984. Ozone formation in laser flash photolysis of oxoacids and oxoanions of chlorine and bromine. J. Chem. Soc. Faraday Trans. 1 80, 2969–2979. https://doi.org/10.1039/F19848002969.

Kolar, B., Arnuš, L., Jeretin, B., Gutmaher, A., Drobne, D., Durjava, M.K., 2014. The toxic effect of oxytetracycline and trimethoprim in the aquatic environment. Chemosphere 115, 75–80. https://doi.org/10.1016/j.chemosphere.2014.02.049.

Kulkarni, P., Chellam, S., 2010. Disinfection by-product formation following chlorination of drinking water: artificial neural network models and changes in speciation with treatment. Sci. Total Environ. 408, 4202–4210. https://doi.org/10.1016/j.scitotenv.2010.05.040.

Kwon, M., Yoon, Y., Kim, S., Jung, Y., Hwang, T.-M., Kang, J.-W., 2018. Removal of sulfamethoxazole, ibuprofen and nitrobenzene by UV and UV/chlorine processes: a comparative evaluation of 275 nm LED-UV and 254 nm LP-UV. Sci. Total Environ. 637–638, 1351–1357. https://doi.org/10.1016/j.scitotenv.2018.05.080.

Lange, N.T., 1999. New mathematical approaches in hydrological modeling — an application of artificial neural networks. Phys. Chem. Earth B 24, 31–35. https://doi.org/10.1016/S1464-1909(98)00007-0.

Le, T.-H., Ng, C., Tran, N.H., Chen, H., Gin, K.Y.-H., 2018. Removal of antibiotic residues, antibiotic resistant bacteria and antibiotic resistance genes in municipal wastewater by membrane bioreactor systems. Water Res. 145, 498–508. https://doi.org/10.1016/j.watres.2018.08.060.

Li, N., Zhang, Y.-H., Xiong, X.-L., Li, Z.-G., Jin, X.-H., Wu, Y.-N., 2005. Study of the physicochemical properties of trimethoprim with β-cyclodextrin in solution. J. Pharm. Biomed. Anal. 38, 370–374. https://doi.org/10.1016/j.jpba.2005.01.014.

Luo, X., Zheng, Z., Greaves, J., Cooper, W.J., Song, W., 2012. Trimethoprim: kinetic and mechanistic considerations in photochemical environmental fate and AOP treatment. Water Res. 46, 1327–1336. https://doi.org/10.1016/j.watres.2011.12.052.

McArthur, R.H., Andrews, R.C., 2015. Development of artificial neural networks based confidence intervals and response surfaces for the optimization of coagulation performance. Water Supply 15, 1079–1087. https://doi.org/10.2166/ws.2015.066.

McGrath, W.D., McGarvey, J.J., 1967. The production, deactivation and chemical reactions of O(1D) atoms. Planet. Space Sci. 15, 427–455. https://doi.org/10.1016/0032-0633(67)90154-7.

Muramoto, Y., Kimura, M., Nouda, S., 2014. Development and future of ultraviolet light-emitting diodes: UV-LED will replace the UV lamp. Semicond. Sci. Technol. 29, 084004. https://doi.org/10.1088/0268-1242/29/8/084004.

NIST, 2002. NDRL/NIST Solution Kinetics Database [WWW Document] URL http://www3.nd.edu/~ndrlrcdc/index.html. (accessed 11.10.19).

Nowell, L.H., Hoigné, J., 1992. Photolysis of aqueous chlorine at sunlight and ultraviolet wavelengths—IIHydroxyl radical production. Water Res. 26, 599–605. https://doi.org/10.1016/0043-1354(92)90233-T.

Qin, L., Lin, Y.-L., Xu, B., Hu, C.-Y., Tian, F.-X., Zhang, T.-Y., Zhu, W.-Q., Huang, H., Gao, N.-Y., 2014. Kinetic models and pathways of ronidazole degradation by chlorination, UV irradiation and UV/chlorine processes. Water Res. 65, 271–281. https://doi.org/10.1016/j.watres.2014.07.041.

Radjenović, J., Petrović, M., Barceló, D., 2009. Fate and distribution of pharmaceuticals in wastewater and sewage sludge of the conventional activated sludge (CAS) and advanced membrane bioreactor (MBR) treatment. Water Res. 43, 831–841. https://doi.org/10.1016/j.watres.2008.11.043.

Rosenfeldt, E., Boal, A.K., Springer, J., Stanford, B., Rivera, S., Kashinkunti, R.D., Metz, D.H., 2013. Comparison of UV-mediated advanced oxidation. J. Am. Water Works Assoc. 105, 29–33.

dos Santos, R. Pires dos, Dean, D.L., Weaver, J.M., Hovanski, Y., 2019. Identifying the relative importance of predictive variables in artificial neural networks based on data produced through a discrete event simulation of a manufacturing environment. Int. J. Model. Simul. 39, 234–245. https://doi.org/10.1080/02286203.2018.1558736.

Sichel, C., Garcia, C., Andre, K., 2011. Feasibility studies: UV/chlorine advanced oxidation treatment for the removal of emerging contaminants. Water Res. 45, 6371–6380. https://doi.org/10.1016/j.watres.2011.09.025.

Sui, Q., Huang, J., Deng, S., Chen, W., Yu, G., 2011. Seasonal variation in the occurrence and removal of pharmaceuticals and personal care products in different biological wastewater treatment processes. Environ. Sci. Technol. 45, 3341–3348. https://doi.org/10.1021/es200248d.

Treinin, A., n.d. The photochemistry of oxyanions. Israel J. Chem. 8, 103–113. https://doi.org/10.1002/ijch.197000018.

Vieno, N.M., Härkki, H., Tuhkanen, T., Kronberg, L., 2007. Occurrence of pharmaceuticals in river water and their elimination in a pilot-scale drinking water treatment plant. Environ. Sci. Technol. 41, 5077–5084. https://doi.org/10.1021/es062720x.

Vilhunen, S., Sillanpää, M., 2010. Recent developments in photochemical and chemical AOPs in water treatment: a mini-review. Rev. Environ. Sci. Biotechnol. 9, 323–330. https://doi.org/10.1007/s11157-010-9216-5.

Vogt, R., Schindler, R.N., 1992. Product channels in the photolysis of HOCl. J. Photochem. Photobiol. Chem. 66, 133–140. https://doi.org/10.1016/1010-6030(92)85207-B.

Wang, D., Bolton, J.R., Hofmann, R., 2012. Medium pressure UV combined with chlorine advanced oxidation for trichloroethylene destruction in a model water. Water Res. 46, 4677–4686. https://doi.org/10.1016/j.watres.2012.06.007.

Wang, W.-L., Wu, Q.-Y., Li, Z.-M., Lu, Y., Du, Y., Wang, T., Huang, N., Hu, H.-Y., 2017. Light-emitting diodes as an emerging UV source for UV/chlorine oxidation: carbamazepine degradation and toxicity changes. Chem. Eng. J. 310, 148–156. https://doi.org/10.1016/j.cej.2016.10.097.

Watts, M.J., Linden, K.G., 2007. Chlorine photolysis and subsequent OH radical production during UV treatment of chlorinated water. Water Res. 41, 2871–2878. https://doi.org/10.1016/j.watres.2007.03.032.

Wu, Z., Fang, J., Xiang, Y., Shang, C., Li, X., Meng, F., Yang, X., 2016. Roles of reactive chlorine species in trimethoprim degradation in the UV/chlorine process: kinetics and transformation pathways. Water Res. 104, 272–282. https://doi.org/10.1016/j.watres.2016.08.011.

Xiang, Y., Fang, J., Shang, C., 2016. Kinetics and pathways of ibuprofen degradation by the UV/chlorine advanced oxidation process. Water Res. 90, 301–308. https://doi.org/10.1016/j.watres.2015.11.069.

Yang, X., Flowers, R.C., Weinberg, H.S., Singer, P.C., 2011. Occurrence and removal of pharmaceuticals and personal care products (PPCPs) in an advanced wastewater reclamation plant. Water Res. 45, 5218–5228. https://doi.org/10.1016/j.watres.2011.07.026.

Yin, R., Ling, L., Shang, C., 2018. Wavelength-dependent chlorine photolysis and subsequent radical production using UV-LEDs as light sources. Water Res. 142, 452–458. https://doi.org/10.1016/j.watres.2018.06.018.

Zhao, Q., Shang, C., Zhang, X., 2009. Effects of bromide on UV/chlorine advanced oxidation process. Water Sci. Technol. Water Supply 9, 627–634. https://doi.org/10.2166/ws.2009.679.